International Journal of Applied Science and Engineering

Experimental and theoretical investigations of prifinium bromide: structural insights, spectroscopic features, topological aspects, and biological properties

S. Selvaraj [1*], A. Ram Kumar [2], A. S. Vickram [2], G. P. Sheeja Mol [3], M. Thirunavukkarasu [4], Mohanraj Kumar [5*]

[1] *Department of Physics, Saveetha School of Engineering, Saveetha Institute of Medical and Technical Sciences (SIMATS), Chennai, Tamil Nadu, India*
[2] *Department Biotechnology, Saveetha School of Engineering, Saveetha Institute of Medical and Technical Sciences (SIMATS), Chennai, Tamil Nadu, India*
[3] *Department of Physics, St. Xavier's College, Thumba, Thiruvananthapuram, Kerala, India*
[4] *Department of Physics, Vel Tech Rangarajan Dr. Sagunthala R and D Institute of Science and Technology, Avadi, Chennai, Tamil Nadu, India*
[5] *Department of Environmental Engineering and Management, Chaoyang University of Technology, Taichung, Taiwan*

ABSTRACT

Prifinium bromide (PB) was analyzed by experimentally and theoretically. The N3-C7 and C6-C7 bonds exceeded standard values due to hyperconjugation, and steric strain. A potential energy surface scan examined dihedral angles ϕ_1 (N3-C22-C23-H51) and ϕ_2 (C7-N3-C22-C23) to assess conformational stability. Vibrational spectra identified key stretching and deformation modes for C-N, C-H, C-C, CH_2, and CH_3 groups. Carbon and proton chemical shifts confirmed the molecular structure with strong correlation between experimental and theoretical values. Theoretical electronic spectra revealed six transitions (482–382 nm), with the most intense absorption at 473 nm (f = 0.0160) corresponding to the H-2 → L (99%) transition, along with the frontier molecular orbital (FMO) energy gap was 3.0501 eV. The most significant stabilization occurs during the π-π* transition from π(C20-C21) to π*(C16-C17) with an energy of 20.75 kJ/mol, while the quaternary nitrogen (-0.38751 e) accumulates electron density, and the bromine (-0.81746 e) exhibits strong electronegativity and electron withdrawing effects. PB did not meet Muegge's rule, and its bioavailability score of 0.55 indicates moderate oral absorption, though poor solubility and low GI absorption may limit systemic exposure. Topological analyses were performed to highlight localized, delocalized, and weak interactions of PB. Molecular docking confirmed PB's anticholinergic potential, showing a binding affinity of -8.6 kcal/mol with the 5ZKC M2 muscarinic receptor.

Keywords: Chemical shifts, DFT, Molecular docking, Topological analysis, Vibrational spectra.

OPEN ACCESS

Received: December 26, 2024
Revised: March 13, 2025
Accepted: March 30, 2025

Corresponding Author:
S. Selvaraj
selvarajs.sse@saveetha.com
Mohanraj Kumar
mohan1991mpt@gmail.com

Publisher:
Chaoyang University of Technology
ISSN: 1727-2394 (Print)
ISSN: 1727-7841 (Online)

1. INTRODUCTION

Quaternary ammonium compounds (QACs) are cationic substances with a broad spectrum of biological activities including disinfectant, antiseptic, biocidal, antimicrobial, and wastewater treatments (Zhang et al., 2015; Hora et al., 2020). Structurally, QACs are nitrogen-containing compounds linked to hydrophobic hydrocarbon chains. The demand for QACs has increased in recent decades due to their expanded use in industrial, textiles, cosmetics, pharmaceutical, and agriculture applications (Vereshchagin et al., 2021; Arnold et al., 2023).

Prifinium bromide (PB), a member of the QAC family, is also known as the 3-(diphenylmethylene)-1,1-diethyl-2-methylpyrrolidin-1-ium bromide. It has the molecular formula $C_{22}H_{28}BrN$, a molecular weight of 386.4 g/mol. Similar to other QACs, PB has permanently charged quaternary nitrogen center, which is expected to enhance

its interaction with biological membranes and contribute to its pharmacological properties. Structurally, PB features a pyrrolidinium ring with three key substituents. The quaternized nitrogen (N^+) at position 1 is bonded to two ethyl ($-C_2H_5$) groups, imparting a permanent positive charge. At position 2, a methyl ($-CH_3$) group influences the steric and electronic properties of the ring. The 3-position carries a diphenylmethylene ($-C(Ph)_2$) group, where a central carbon is bonded to two phenyl rings (C_6H_5). Bromide (Br^-) counterion stabilizes the positive charge on nitrogen.

As a QAC, PB exhibits anticholinergic, antispasmodic, and antiemetic effects, making it useful in treating gastrointestinal disorders, including bowel and colon syndromes (Kumada et al., 1970; Moayyedi et al., 2019). PB has demonstrated anticholinergic effect in eighteen individuals, showing notable benefits for patients with irritable bowel syndrome (Piai et al., 1979). The quantification of PB in biological blood and urine samples following intravenous or oral administration has been reported earlier (Tokuma et al., 1982). Additionally, pre-administration of PB mitigates the side effects such as vomiting, excessive salivation, and diarrhea induced by fenprostalene in female beagles (Moriyoshi et al., 1999). Furthermore, PB shows an antispasmodic effect by inhibiting Prostigmin-induced hypermotility in patients with diverticular disease (Sasaki et al., 1981). Beyond its role in gastrointestinal and colon disorders, PB is also used to inhibit urinary bladder contractions in rats and guinea pigs (Terai et al., 1991). Spectroscopic techniques have been utilized to quantify the PB in film-coated tablets within pharmaceutical formulations (Abu Nameh et al., 2013). The identification of PB by high-performance liquid chromatography (HPLC) and thin-layer chromatography (TLC) has been previously documented (Musumarra et al., 1987; Sasa et al., 1988; Amro, 2019). In addition, the combination of PB and paracetamol has been quantified using the bivariate method in the pharmaceutical samples (Lataifeh et al., 2014).

A comprehensive literature review reveals that only a few studies have addressed the biological and analytical determination of PB. Nevertheless, there have been no reports of theoretical and experimental spectroscopic analyses conducted on PB. Therefore, this study integrates both approaches to investigate its structural, biological, topological, and spectroscopic properties.

2. MATERIALS AND METHODS

2.1 Sample and Experimental Details

The powder form of PB (97% purity) was purchased from a leading chemical supplier and used without further modification for spectral measurements. The FT-IR and FT-Raman spectra were recorded within the spectral range of 4000-400 cm^{-1} using a Perkin Elmer Spectra two FT-IR/ATR spectrometer and a Bruker RFS 27 Standalone FT-Raman Spectrometer, with 0.5 and 2 cm^{-1} resolutions, respectively. The chemical shift of ^1H and ^{13}C were recorded in deuterated DMSO using a Bruker high-resolution nuclear magnetic resonance spectrometer at the 300 K with Tetramethylsilane (TMS) as an internal reference. The electronic spectrum was captured in the UV-Vis region using a Perkin Elmer Lambda 35 UV Winlab V 6.0 spectrometer with a bandwidth of 0.5–4.0 nm.

2.2 Computational Details

The theoretical calculations for PB were performed at the DFT/B3LYP level of theory with the 6-31++G(d,p) basis set (Kohn et al., 1965; Lee et al., 1988; Becke, 1993) using the Gaussian 09 W program suite (Frisch et al., 2009). Vibrational assignments for PB were carried out using the chemcraft program (Zhurko et al., 2009), which provides a more precise graphical representation. The chemical shifts of ^1H and ^{13}C in the gas phase were calculated using the gauge-including atomic orbital (GIAO) approach (Petersilka et al., 1966). The electronic properties of PB were simulated using the Time-dependent density functional theory (TD-DFT) approach (Runge et al., 1984). Topological analysis was conducted using Multiwfn software, and the results were visualized with the VMD program (Humphrey et al., 1996; Lu et al., 2012). Molecular docking simulations were performed using AutoDock4 software (Morris et al., 2009), and the resulting ligand-protein complex was visualized with the PyMol and LigPlot$^+$ tools (Wallace et al 1995; DeLano, 2002).

3. RESULTS AND DISCUSSION

3.1 Optimized Structural Parameters

The optimized structural parameters of PB, including bond angles and lengths, were simulated in the gas phase and are detailed in Table 1. The molecular structure with complete atom numbering is illustrated in Fig. 1. The optimized structure of PB comprises twenty-eight C-H, one C-N, three N-C, and twenty-one C-C bond distances. Additionally, it features six C-N-C, four N-C-C, one C-C-N, forty C-C-H, thirteen H-C-H, twenty-five C-C-C, and seven N-C-H bond angles.

The bond distances of N3-C4, N3-C7, N3-C22, and C2-N3 were computed as 1.527, 1.552, 1.515, and 1.548 Å, respectively. The N3-C7 bond was the longest due to hyperconjugation and steric strain. The C7 methine carbon, attached to a methyl group, underwent hyperconjugation, weakening and elongating the bond. Steric strain within the pyrrolidinium ring further reduced orbital overlap, contributing to its elongation. While nitrogen's electronegativity typically shortens bonds, the electron-donating methyl group at C7 counteracted this effect, resulting in a longer N3-C7 bond. The bond lengths of C-H in the diphenyl structure ranged between 1.085 and 1.087 Å, whereas the bond length of C7-H33 was calculated as 1.096 Å. Similarly, the bond distances of C-H in methyl and methylene group of the diethyls and a pyrrolidine structure

were simulated within 1.090–1.095 Å and 1.090–1.100 Å, respectively. In this case, C2-H27 (1.100 Å) is the longest C-H bond due to its sp^3 hybridization in the diethyl and pyrrolidinium moieties, while C11-H37 (1.085 Å) is the shortest due to its sp^2 hybridization in the diphenyl moiety, compared to other C-H bonds. The bond lengths of C-C bonds were computed within 1.353–1.535 Å. The C6-C9 bond (1.353 Å) is shorter than a typical C-C bond due to conjugation, as C9 bridges two phenyl rings, introducing partial double-bond character that strengthens the bond. Structural constraints within the pyrrolidinium ring also contribute to its contraction. In contrast, the C6-C7 bond (1.535 Å) is the longest, slightly exceeding a standard C-C single bond due to similar effect of N3-C7 bond elongation without any opposing influence.

The bond angles of C-N-C, N-C-C, and N-C-H in the methyl pyrrolidine structure were simulated within the 101.9–112.3°, 103.3–114.4°, and 103.3–106.9°, respectively, indicating deviations due to ring strain and steric interactions. The C1-C2-N3 bond angle was calculated as 117.3°, slightly larger than the expected value for sp^3-hybridized carbon, possibly due to the electronic effects of nitrogen. The H-C-H bond angles in the methylene and methyl groups of the diethyl chains attached to nitrogen were found within 107.7–108.1° and 106.4–109.1°, respectively. In contrast, within the methyl pyrrolidine structure, H-C-H bond angles in the methylene and methyl groups ranged from 106.6–111.3° and 107.4–109.3°, respectively, indicating slight deviations due to ring constraints. The C-C-H bond angles were computed within 105.9–120.2°, while the C-C-C bond angles ranged from 103.7–126.4°. Notably, the expanded bond angles beyond 120°, particularly in the conjugated diphenyl methylene system, suggest electron delocalization effects. Additionally, some compressed angles, such as those around the pyrrolidinium ring, may arise from steric hindrance and ring strain.

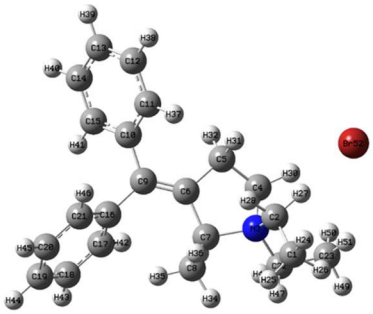

Fig. 1. Optimized molecular structure of PB

3.2 Potential Energy Surface Scans

A potential energy surface (PES) scan was conducted for the PB compound with a fixed N-terminus position. After optimizing the PB structure (Fig. 1), a rigid potential energy surface scan was conducted by rotating molecular groups from 0° to 360° in 10° increments, focusing on the dihedral angles ϕ_1(N3-C22-C23-H51) and ϕ_2(C7-N3-C22-C23) relative to the N3-C22 and C7-N3 bonds in the gas phase. The scan results, presented as plots of scan angle versus relative energy (kcal/mol) in Figs. 2(a) and (b), provide crucial insights into the stability and flexibility of PB. Also, the calculated conformational energies are presented in Table S1 (supplementary material), along with the corresponding scan coordinates. Rotation of ϕ_1 (Fig. 2(a)) revealed four stable lowest-energy conformers at 50°, 130°, 240°, and 370°, each with an energy of approximately -2,184,703 kcal/mol, whereas three unstable highest-energy conformers were observed at 70°, 190°, and 310°, with an energy of approximately -2,184,701 kcal/mol. Notably, the most stable conformer (conformer I) was identified at 130°, 240°, and 370°, all exhibiting identical energy levels, indicating symmetrical stability in these positions. Similarly, rotation of ϕ_2 (Fig. 2(b)) led to three stable lowest-energy conformers at 167°, 307°, and 407°, with energy values ranging from -2,184,699.66 to -2,184,703.76 kcal/mol, while the three unstable highest-energy conformers were found at 247°, 357°, and 467°, with energy values between -2,184,691.14 and -2,184,696.78 kcal/mol. The most stable conformer (conformer I) was observed at 167° and 527°, both maintaining an identical energy of -2,184,703.7 kcal/mol, suggesting a preferred molecular conformation.

From rotations of dihedral angles ϕ_1(N3-C22-C23-H51) and ϕ_2(C7-N3-C22-C23), a stable conformer (conformer I) was identified, exhibiting the identical energy levels (-2184703.79 kcal mol^{-1}) but different positional orientations. This indicates multiple occurrences of the same stable structural arrangement at different dihedral angles. Figs. 3(a–c) and (a'–c') illustrate the lowest-energy stable conformers (I, II, and III) and the highest-energy unstable conformers (I', II', and III') at the identified rotational dihedral angles as discussed.

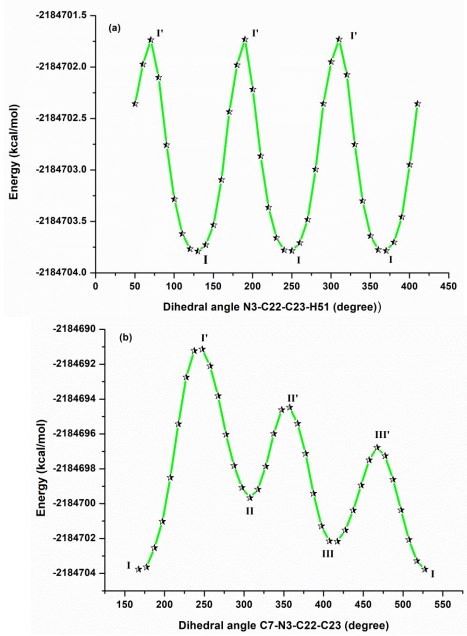

Fig. 2. PES scan of NCCH and CNCC dihedral angles of PB

Table 1. Optimized geometrical parameters of PB

Bond lengths (Å)	Values	Bond lengths (Å)	Values	Bond lengths (Å)	Values
C1-C2	1.524	C6-C9	1.353	C14-H40	1.086
C1-H24	1.095	C7-C8	1.527	C15-H41	1.086
C1-H25	1.092	C7-H33	1.096	C16-C17	1.405
C1-H26	1.092	C8-H34	1.093	C16-C21	1.405
C2-N3	1.548	C8-H35	1.090	C17-C18	1.398
C2-H27	1.100	C8-H36	1.092	C17-H42	1.087
C2-H28	1.090	C9-C10	1.497	C18-C19	1.397
N3-C4	1.527	C9-C16	1.497	C18-H43	1.086
N3-C7	1.552	C10-C11	1.405	C19-C20	1.399
N3-C22	1.515	C10-C15	1.407	C19-H44	1.086
C4-C5	1.520	C11- C12	1.396	C20-C21	1.396
C4-H29	1.095	C11- H37	1.085	C20-H45	1.086
C4-H30	1.099	C12- C13	1.397	C21-H46	1.086
C5-C6	1.522	C12- H38	1.086	C22-C23	1.527
C5-H31	1.095	C13- C14	1.398	C22-H47	1.091
C5-H32	1.093	C13- H39	1.086	C22-H48	1.094
C6-C7	1.535	C14-C15	1.395	C23-H49	1.095
C23- H50	1.092	C23- H51	1.092	-	-
Bond angles (°)	**Values**	**Bond angles (°)**	**Values**	**Bond angles (°)**	**Values**
C2-C1-H24	105.9	H29-C4-H30	111.3	C12-C13-C14	119.6
C2-C1-H25	114.9	C6-C5-H31	113.9	C12-C13-H39	120.2
C2-C1-H26	112.5	C6-C5-H32	111.9	C14-C13-H39	120.2
C1-C2-N3	117.3	C5-C6-C7	108.1	C13-C14-C15	120.2
C1-C2-H27	109.2	C5-C6-C9	125.2	C13-C14-H40	120.1
C1-C2-H28	110.4	H31-C5-H32	106.6	C15-C14-H40	119.7
H24-C1-H25	107.6	C7-C6-C9	126.4	C14-C15-C41	119.6
H24-C1-H26	106.4	C6-C7-C8	117.7	C17-C16-C21	118.4
H25-C1-H26	109.1	C6-C7-H33	109.3	C16-C17-C18	120.9
N3-C2-H27	105.8	C6-C9-C10	121.1	C16-C17-H42	119.4
N3-C2-H28	105.5	C6-C9-C16	123.6	C16-C21-C20	120.8
C2-N3-C4	108.1	C8-C7-H33	108.3	C16-C21-H46	119.3
C2-N3-C7	112.2	C7-C8-H34	111.3	C18-C17-H42	119.7
C2-N3-C22	112.3	C7-C8-H35	108.9	C17-C18-C19	120.1
H27-C2-H28	108.1	C7-C8-H36	112.1	C17-C18-H43	119.8
C4-N3-C7	101.9	H34-C8-H35	107.4	C19-C18-H43	120.2
C4-N3-C22	110.4	H34-C8-H36	109.3	C18-C19-C20	119.6
N3-C4-C5	103.3	H35-C8-H36	107.7	C18-C19-H44	120.2
N3-C4-H29	106.4	C10-C9-C16	115.2	C20-C19-H44	120.2
N3-C4-H30	109.7	C9-C10-C11	121.5	C19-C20-C21	120.2
C7-N3-C22	111.3	C9-C10-C15	120.2	C19-C20-H45	120.0
N3-C7-C6	103.5	C9-C16-C17	120.8	C21-C20-H45	119.7
N3-C7-C8	113.8	C9-C16-C21	120.7	C20-C21-H46	119.9
N3-C7-H33	103.3	C11-C10-C15	118.3	C23-C22-H47	111.5
N3-C22-C23	114.4	C10-C11-C12	120.9	C23-C22-H48	110.3
N3-C22-H47	106.9	C10-C11-H37	119.6	C22-C23-H49	108.0
N3-C22-H48	105.8	C10-C15-C14	120.9	C22-C23-H50	111.9
C5-C4-H29	111.8	C10-C15-H41	119.5	C22-C23-H51	113.3
C5-C4-H30	113.8	C12-C11-H37	119.5	H47-C22-H48	107.7
C4-C5-C6	103.7	C11-C12-C13	120.2	H49-C23-H50	108.1
C4-C5-H31	109.1	C11-C12-H38	119.6	H49-C23-H51	108.9
C4-C5-H32	111.7	C13-C12-H38	120.2	H50-C23-H51	106.5

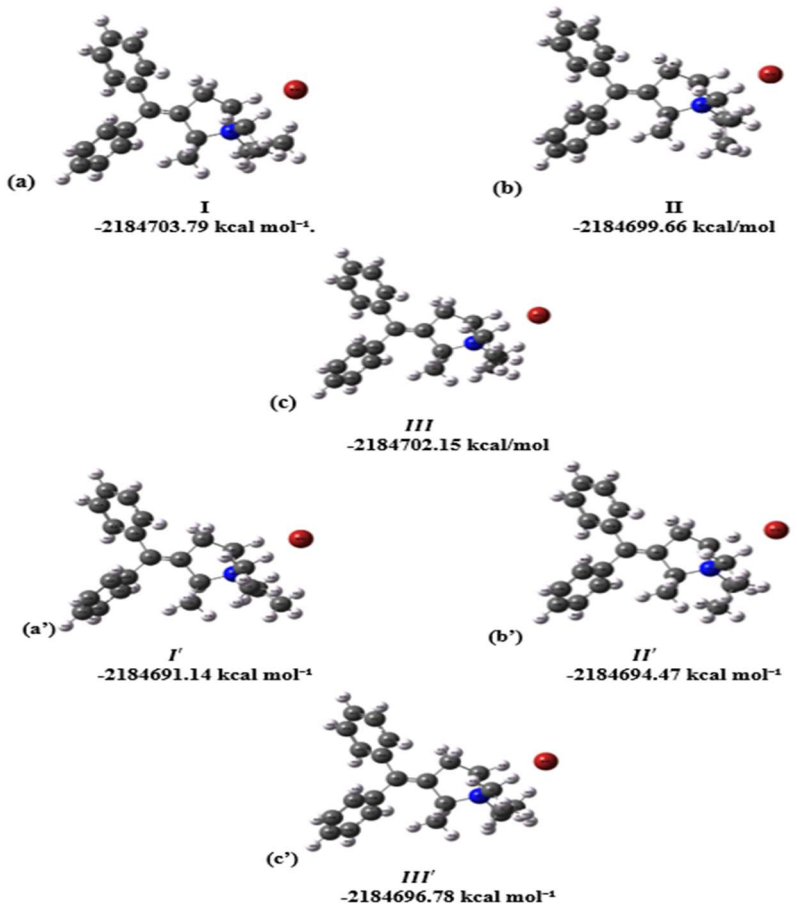

Fig. 3. Highest and lowest energy conformations of PB upon NCCH and CNCC rotation: (a)–(c) represent minima, while (a')–(c') correspond to maxima in the energy profile

3.3 Vibrational Properties

PB consists of 52 atoms, exhibits 150 fundamental vibrational modes following the (3N−6) rule for vibrational degrees of freedom, and is expected to have C_1 point group symmetry. The experimental and theoretical wavenumbers, along with their corresponding vibrational modes, are presented in Table S2 (supplementary material), while the associated vibrational spectra are shown in Figs. 4 and 5.

3.3.1 CH Vibrations

The CH group exhibits two distinct types of vibrations: stretching and deformations. Typically, CH stretching frequencies range between the 3100–3000 cm^{-1} (Rama et al., 2023; Vijayalakshmi et al., 2024), which remains unaffected by the compound's physical nature, making it a characteristic region for CH stretching vibrations. In this study, theoretical simulations yielded CH stretching vibrations at 3085, 3083, 3078, 3073, 3071, 3067, 3064, 3059, 3056, 3052, 3045, 3035, and 2927 cm^{-1}. Experimentally, a single band was detected at 3046 cm^{-1} in the FT-Raman spectrum and at 3032 cm^{-1} in the FT-IR spectrum. The in-plane deformation of CH group typically spans the range of 1450–1000 cm^{-1}. Theoretical calculations yielded frequencies between 1557 and 1006 cm^{-1}, which align with experimental peaks at 1511, 1415, 1335, 1286, 1235, 1138, 1051 cm^{-1} in the FT-IR spectrum and at 1301, 1161, 1027 cm^{-1} in the FT-Raman spectrum. For out-of-plane deformation, a few bands were detected in the range of 1000–750 cm^{-1} (Divya et al., 2024). The theoretical spectrum exhibited bands between 982 and 740 cm^{-1}, showing good agreement with observed FT-Raman and FT-IR bands at 998, 744 cm^{-1}, and at 954, 849, 733 cm^{-1}, respectively.

3.3.2 CN and CC Vibrations

Identifying CN stretching modes is challenging due to the overlap of multiple peaks within a similar spectral region. In aromatic compounds, CN vibrations typically occur between 1382 and 1266 cm^{-1} (Silverstein et al., 1962). In a previous study on 2-trifluoromethyl benzimidazole, these bands were observed at 1461, 1365, 1286, and 1168 cm^{-1} (Ram Kumar et al., 2023). Similarly, for PB, theoretical simulations predicted bands at 1285, 1277, and 1225 cm^{-1}, which are in good agreement with the experimental bands at 1286 and 1235 cm^{-1} in the FT-IR spectrum.

CC stretching vibrations play a crucial role in aromatic

compounds and are commonly observed between 1650 and 1100 cm^{-1} (Jeba Reeda et al., 2025). Theoretical analysis of PB revealed bands at 1617, 1583, 1580, 1558, 1557, 1473 and 1248 cm^{-1}, which align well with experimental bands at 1688, 1611, 1585, 1511, and 1477 cm^{-1} in the FT-IR spectrum, and at 1656 and 1596 cm^{-1} in the FT-Raman spectrum.

3.3.3 CH_2 Vibrations

The methylene (CH_2) group exhibits asymmetric and symmetric stretching vibrations, typically occurring within the range of 3100–3000 cm^{-1} and 3000–2900 cm^{-1}, respectively (Selvaraj et al., 2022). For PB, theoretical calculations indicated asymmetric stretching vibrations between 3035 and 2973 cm^{-1}, which align with experimental bands at 3032 cm^{-1} (FT-IR) and 2990 cm^{-1} (FT-Raman). Symmetric stretching was noted at 2956, 2952, 2870, and 2833 cm^{-1} in theoretical calculations, with an experimental band at 2953 cm^{-1} in the FT-IR spectrum. Deformations such as rocking, scissoring, wagging, and twisting typically occur below 1500 cm^{-1} (Rajkumar et al., 2018). In this investigation, CH_2 scissoring modes were predicted at 1473, 1468, 1467, and 1429 cm^{-1} in theoretical calculations, which corresponds to experimental bands at 1477 and 1441 cm^{-1} in the vibrational spectra. Additionally, CH_2 wagging modes were found at 1409, 1390, 1373, 1360, and 1350 cm^{-1} in theoretical calculations. The CH_2 rocking modes were predicted below 1134 cm^{-1}, with experimental peaks were observed at 849, 804, and 733 cm^{-1} in the FT-IR spectrum and at 1027, 998, and 615 cm^{-1} in the FT-Raman spectrum. CH_2 twisting modes were simulated between 1324 and 1053 cm^{-1}, showing good correlation with experimental peaks at 1335, 1286, 1096, and 1051 cm^{-1} in the FT-IR spectrum and at 1177 cm^{-1} in the FT-Raman spectrum.

3.3.4 CH_3 Vibrations

PB contains three methyl (CH_3) groups, which exhibits nine fundamental vibrations. Symmetric and asymmetric CH_3 stretching are typically observed around 2870 and 2890 cm^{-1} (Ram Kumar et al., 2023). Theoretical calculations yielded symmetric stretching frequencies at 2951, 2944, and 2941 cm^{-1}, with an experimental band at 2942 cm^{-1} in the FT-Raman spectrum. For asymmetric stretching, theoretical simulations resulted in values of 3045, 3022, 3017, and 3001 cm^{-1}, with a single experimental band at 3046 cm^{-1} in the FT-Raman spectrum. Asymmetric and symmetric CH_3 deformations occur within the range of 1465–1440 cm^{-1} and 1390–1370 cm^{-1}, respectively (Ram Kumar et al., 2024). Theoretical spectra showed asymmetric deformation bands between 1473 and 1429 cm^{-1}, aligning well with experimental values at 1477 cm^{-1} (FT-IR) and 1441 cm^{-1} (FT-Raman). Similarly, the theoretical symmetric deformation was found within 1409–1324 cm^{-1}, with an experimental band at 1335 cm^{-1} in the FT-IR spectrum.

3.4 Chemical Shifts

The observed ^1H and ^{13}C NMR spectra are shown in Fig. 6(a) and (b), with atomic numbering in Fig. 1 and chemical shifts listed in Table 2. Aromatic hydrogens typically exhibit shifts between 8.00 and 7.00 ppm (Selvaraj et al., 2018), while aromatic carbons appear between 100 and 150 ppm (Ram Kumar et al., 2021). In this study, the methyl protons H24–H26, H34–H36, and H49–H51 of the diethyl groups and pyrrolidine ring showed experimental shifts ranging from 1.251 to 1.13 ppm, while theoretical values varied from 3.082 to 1.086 ppm. Correspondingly, the methyl carbons C1, C8, and C23 exhibited experimental shifts between 8.7 and 15.26 ppm, with theoretical values ranging

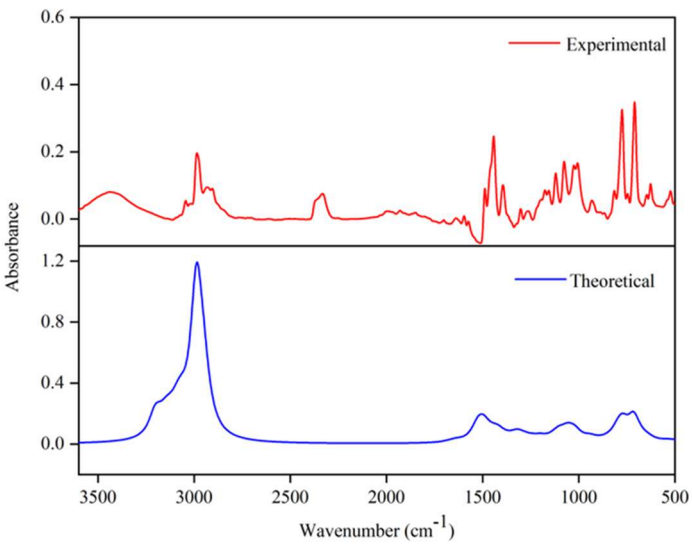

Fig. 4. Simulated and experimental FT-IR spectra of PB

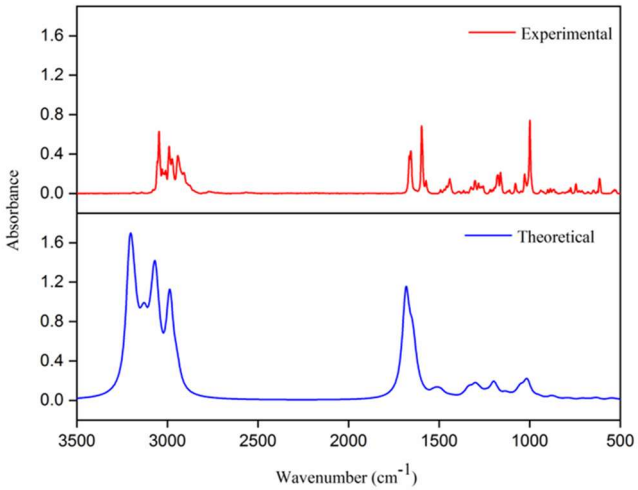

Fig. 5. Simulated and experimental FT-Raman spectra of PB

from 2.964 to 5.233 ppm. The methylene protons H27–H32 and H47–H48, associated with the diethyl groups and pyrrolidine ring, exhibited experimental shifts between 3.796 and 2.592 ppm, while theoretical values ranged from 9.315 to 2.484 ppm. Similarly, the methylene carbons C2, C4, C5, and C22 showed experimental shifts from 25.92 to 57.46 ppm, with theoretical values between 24.543 and 53.029 ppm. These variations reflect the influence of the nitrogen center in the pyrrolidinium ring and steric interactions within the diethyl group. The methine proton H33 had an experimental shift of 4.17 ppm, closely aligning with the theoretical value of 4.306 ppm. The methine carbon C7 followed a similar trend, with experimental and theoretical shifts of 70.85 and 72.345 ppm, respectively, indicating moderate de-shielding due to nitrogen attachment. The diphenyl ring protons H37–H46 appeared at the 7.420–7.233 ppm experimentally, aligning well with theoretical values of 7.981–7.124 ppm. The diphenyl carbons C10 to C21 exhibited significant shifts due to conjugation and extended π-electron delocalization. Experimental shifts ranged from 128.47 to 141.34 ppm, while theoretical values were slightly lower, ranging from 114.216 to 130.798 ppm. Notably, C10 and C16, with experimental shifts of 141.34 and 141.18 ppm and theoretical shifts of 130.798 and 130.77 ppm, respectively, showed the largest deviations, likely due to resonance effects within the phenyl rings. The bridge carbon C9, linking the diphenyl and pyrrolidinium rings, had an experimental shift of 139.75 ppm and a theoretical value of 133.613 ppm, indicating a strong electronic influence from both rings. Similarly, C6, bonded to C9, exhibited an experimental shift of 135.49 ppm and a theoretical value of 127.031 ppm, highlighting interactions with adjacent methylene and phenyl groups.

Table 2. Experimental and theoretical ^{1}H and ^{13}C chemical shifts of PB

Category	Atoms	Experimental (ppm)	Theoretical (ppm)
		^{1}H NMR	
Phenyl	H37–H 46 (10) H24–H26 (3)	7.420–7.233	7.981–7.124
Methyl	H34–H36 (3) H49–H51 (3)	1.251–1.13	3.082–1.086
Methione	H33 (1)	4.17	4.306
Methylene	H27–H32 (6) H47–H48 (2)	3.796–2.592	9.315–2.484
		^{13}C NMR	
Phenyl	C10–C21 (12)	141.34–128.47	130.798–114.216
Methyl	C1, C8, C23 (3)	15.26–8.7	5.233–2.964
Methione	C7 (1)	70.85	72.345
Methylene	C2, C4, C5, C22 (4)	57.46–25.92	53.029–24.543
Others	C9, C6 (2)	139.75, 135.49	133.613, 127.031

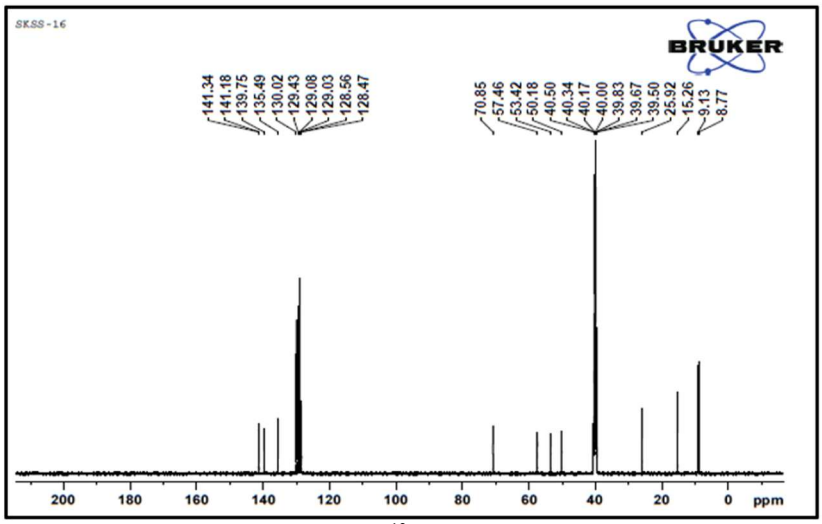

Fig. 6(a). Experimental ^{13}C NMR spectrum of PB

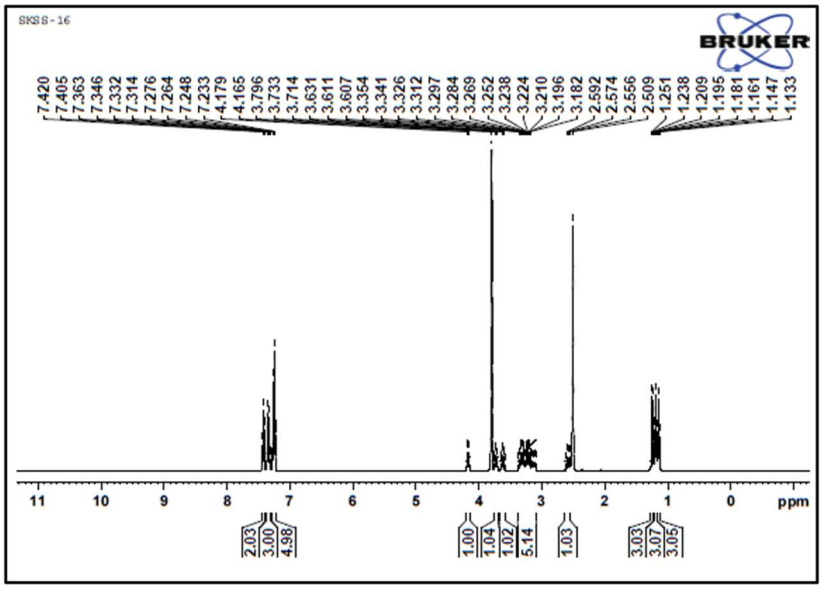

Fig. 6(b). Experimental ^{1}H NMR spectrum of PB

3.5 Electronic Properties

The theoretical electronic spectra of PB reveal six major transitions at 482, 477, 473, 388, 385, and 382 nm, with excitation energies ranging from 2.567 to 3.245 eV. Among these, most intense absorption occurs at 473 nm (f = 0.0160), corresponding to the H-2 → L (99%) transition, indicating a high probability of excitation. In contrast, the transitions at 482 nm (f = 0.0010) and 477 nm (f = 0.0022), attributed to H → L (99%) and H-1 → L (98%), respectively, exhibit significantly lower oscillator strengths, suggesting weaker absorption. At higher energies, transitions involving the LUMO+1 orbital show a significant drop in oscillator strengths. For instance, the H → L+1 (99%) transition at 388 nm has f = 0, meaning this transition is formally forbidden or extremely weak in absorption. Similarly, the transitions at 385 nm (H-1 → L+1, f = 0.0003) and 382 nm (H-1 → L+1, f = 0.0002) exhibit very low oscillator strengths, contributing minimally to the overall absorbance spectrum. Experimentally, PB exhibits a strong absorption peak at 379 nm with an absorbance of 1.3019, suggesting a significant electronic transition. This closely matches the theoretical transitions at 382, 385, and 388 nm, corresponding to H → L+1 and H-1 → L+1 transitions.

The calculated frontier molecular orbitals (FMO) and additional electronic characteristics in the gas phase are presented in Table S3 (supplementary material) and depicted in Fig. 7. The highest occupied molecular orbital (HOMO) energy is -8.0363 eV, while the lowest unoccupied molecular orbital (LUMO) energy is -4.9862 eV, resulting in a HOMO-LUMO energy gap of 3.0501 eV, which indicates moderate chemical stability and potential electronic transitions. The ionization potential (8.0363 eV) suggests PB is resistant to electron loss, whereas its electron affinity (4.9862 eV) reflects a significant tendency to accept

electrons, reinforcing its electrophilic nature. The chemical hardness (1.5250 eV) implies resistance to electronic deformation, while the chemical softness (0.3278 eV^{-1}) suggests some degree of reactivity. An electrophilicity index (13.9002 eV) confirms PB's solid electron-accepting nature, and its maximum electron charge transfer (4.2696 eV) suggests significant charge exchange capability. Furthermore, the electronegativity and negative chemical potential reinforce PB's strong affinity for electrons. In the FMO visualization, the green and red color distributions represent the negative and positive phases, respectively. Additionally, the simulated density of states (DOS) spectra for PB were generated and are shown in Fig. 8. The DOS spectra illustrate green for occupied orbitals and red for unoccupied orbitals, providing insights into the FMO energy gap, electronic distribution, and chemical reactivity of PB. Table 3 presents the electronic spectral properties of PB in the gas phase, while Figs. 9 and 10 illustrate the simulated and experimental Ultraviolet-Visible (UV-Vis) spectra, respectively.

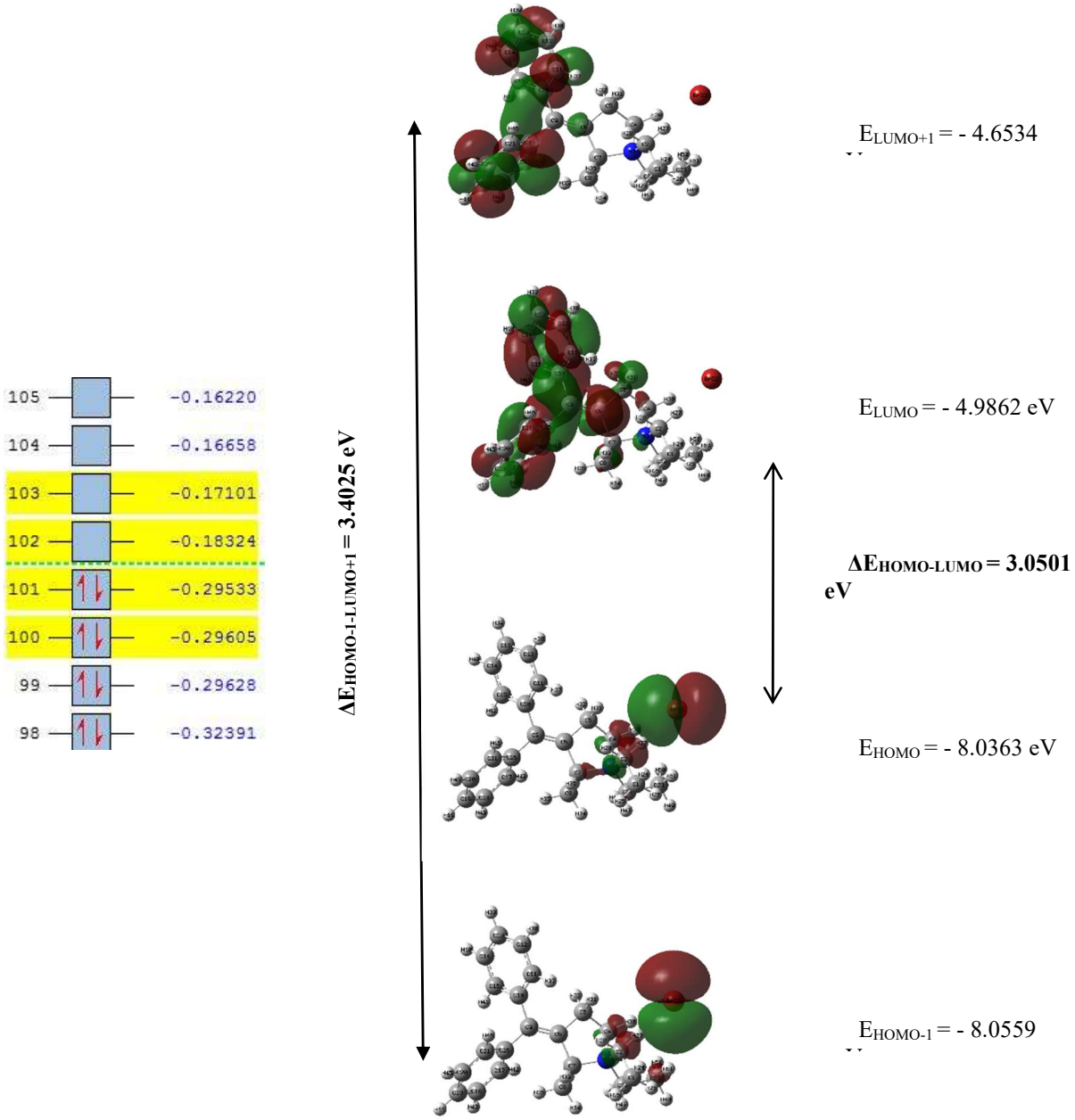

Fig. 7. Simulated FMO plots of PB

Table 3. Calculated wavelengths (λ), excitation energies (E), oscillator strengths (f) and major contributions of PB

λ (nm)	E (eV)	f	Major contributions
482	2.567	0.0010	H→L (99%)
477	2.593	0.0022	H-1→L (98%)
473	2.620	0.0160	H-2→L (99%)
388	3.194	0	H→L+1 (99%)
385	3.220	0.0003	H-1→L+1 (99%)
382	3.245	0.0002	H-1→L+1 (98%)

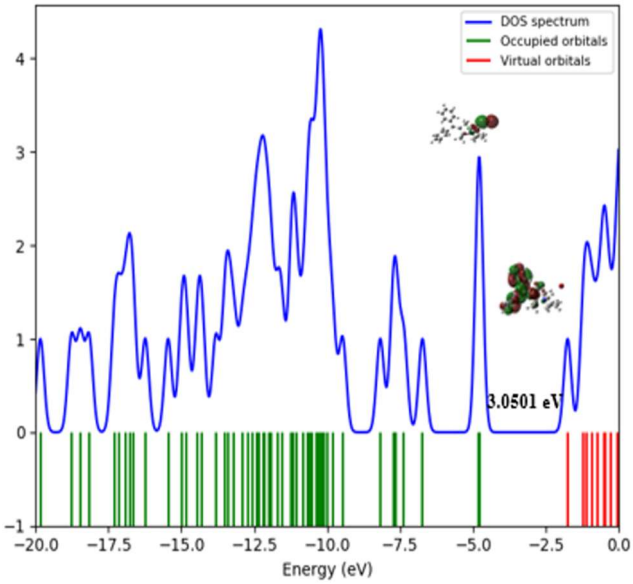

Fig. 8. Simulated DOS spectrum of PB

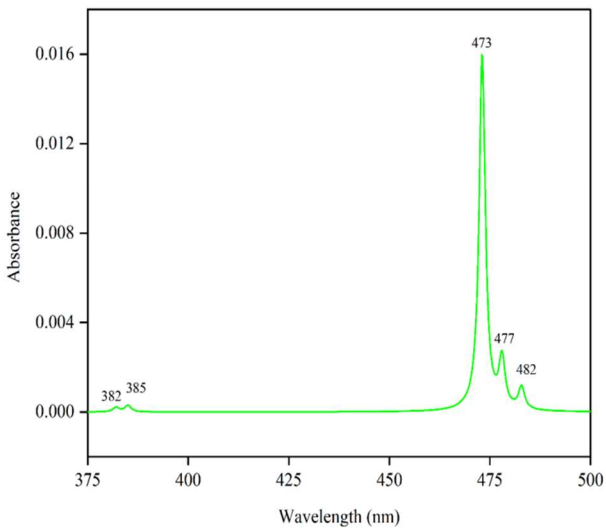

Fig. 9. Simulated electronic spectrum of PB

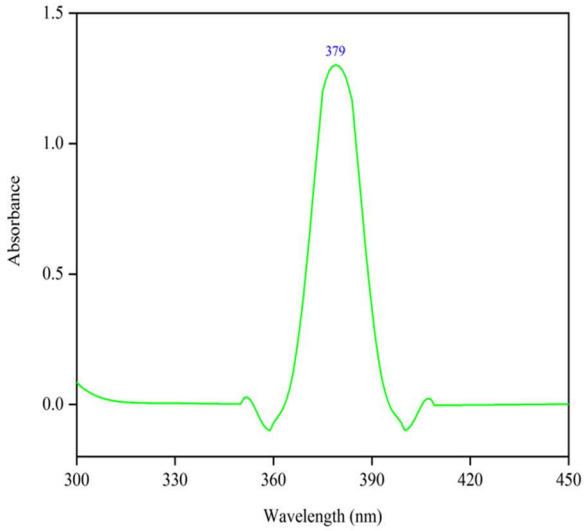

Fig. 10. Experimental electronic spectrum of PB

3.6 Natural Bond Orbital Study

The Natural Bond Orbital (NBO) study provides an accurate representation of the natural Lewis structure by selecting orbital features that maximize electron density (Thirunavukkarasu et al., 2022). The NBO technique, based on the second-order Fock matrix, was used to evaluate donor-acceptor interactions in PB. The simulated NBO parameters are presented in Table 4. The most significant stabilization occurs during the π-π* transition involving π (C20-C21) → π*(C16-C17), enhancing its stability with an associated energy of 20.75 kJ/mol. Other notable π-π* interactions include transitions from C12-C13, C16-C17, and C20-C21 (donors) to C10-C11, and C18-C19 (acceptors), with stabilization energies of 20.64, 20.25, and 20.1 kJ/mol, respectively. Lone pair (LP) transitions were also observed, such as LP(n) Br52 → σ*(C2-H27) and LP(n) Br52 → σ*(C4-H30), with energy values of 12.33 and 9.31 kJ/mol. The NBO study confirms that the total electron density is distributed as 98.335% Lewis structure and 1.665% non-Lewis's structure, indicating strong classical bonding. As shown in Table 4, the transitions LP(n) Br52 → σ*(C2-H27) and LP(n) Br52 → σ*(C4-H30) exhibit polarization energies of 0.083 and 0.072 a.u., respectively. This is attributed to the electronegative bromide ion, which are weakly bonded in this structure, leading to notable polarization effects.

3.7 Mulliken Charges and MEP Surfaces

The Mulliken population analysis and Molecular Electrostatic Potential (MEP) surface of PB mapping reveals variations in charge distribution, reactive sites, influencing its electronic properties and reactivity. Mulliken charges, developed by Robert S. Mulliken, are widely used in quantum chemical calculations to describe electron density variations across atomic sites. The predicted Mulliken charge distribution of PB is presented in Table S4 (supplementary material) and graphically visualized in the Fig. 11, while the MEP surface is depicted in Fig. 12.

The quaternary nitrogen atom carries a charge of -0.38751e, indicating electron density accumulation within the pyrrolidinium ring, whereas bromide exhibits the highest negative charge of -0.81746e, reflecting its strong electronegativity and electron-withdrawing nature. Among the carbon atoms, C1 (-0.67562 e), C7 (-0.65352 e) and C23 (-0.58077 e) exhibit the most negative charges, suggesting localized electron density, whereas C2, C6, C10, C12, C14, C17 and C22 carry positive charges, contributing to molecular charge redistribution. Additionally, C5, C8, C9, C11, C13, C15, C16, C18, C19, C20, C21, and C23 have negative charges, influencing the overall electronic stability of the molecule. The hydrogen atoms predominantly carry positive charges, with H30 (0.242657 e), H31 (0.285895 e), H33 (0.233862 e), and H51 (0.250806 e) being the most polarized, suggesting electrostatic interactions and potential hydrogen bonding, particularly near the quaternary ammonium center. The MEP surface map, which visually represents electron density distribution, aligns with the Mulliken charge analysis by confirming the electrophilic and nucleophilic sites within PB. The electron-deficient regions appear as white areas around hydrogen atoms, indicating their susceptibility to electrophilic attack, while electron-rich regions are depicted in red around the bromide ion due to its high electronegativity, making it favorable for nucleophilic interactions.

Table 4. Second-order perturbation theory of Fock matrix selected NBO analysis of PB

Donor (i)	Acceptor (j)	Type of transition	Occupancy (ED/e)		$E^{(2)a}$ KJ/mol	E(j)-E(i)[b] a.u	F(i,j)[c] a.u
			Donor (i)	Acceptor (j)			
C20-C21	C16-C17	π-π*	1.6588	0.3619	20.75	0.28	0.068
C12-C13	C10-C11	π-π*	1.6520	0.3629	20.64	0.28	0.068
C16-C17	C18-C19	π-π*	1.6592	0.3268	20.25	0.28	0.067
C20-C21	C18-C19	π-π*	1.6588	0.3268	20.1	0.28	0.067
C14-C15	C12-C13	π-π*	1.6647	0.3252	19.92	0.28	0.067
C12-C13	C14-C15	π-π*	1.6520	0.3164	19.91	0.28	0.067
C10-C11	C12-C13	π-π*	1.6481	0.3252	19.87	0.28	0.067
C18-C19	C16-C17	π-π*	1.6600	0.3619	19.87	0.28	0.067
C14-C15	C10-C11	π-π*	1.6647	0.3629	19.76	0.28	0.067
C18-C19	C20-C21	π-π*	1.6600	0.3113	19.7	0.28	0.067
C10-C11	C14-C15	π-π*	1.6481	0.3164	19.4	0.28	0.066
C16-C17	C20-C21	π-π*	1.6592	0.3113	18.74	0.28	0.065
Br52	C2-H27	LP (n)-σ*	1.9088	0.0604	12.33	0.68	0.083
Br52	C4-H30	LP (n)-σ*	1.9088	0.0525	9.31	0.69	0.072

[a]$E^{(2)}$ - Energy of the hyper-conjugative interaction (stabilization energy) energy.
[b]E(j)-E(i) - The energy difference between the donor (i) and acceptor (j) orbitals.
[c]F(i,j)- the fork matrix element between i and j NBO.

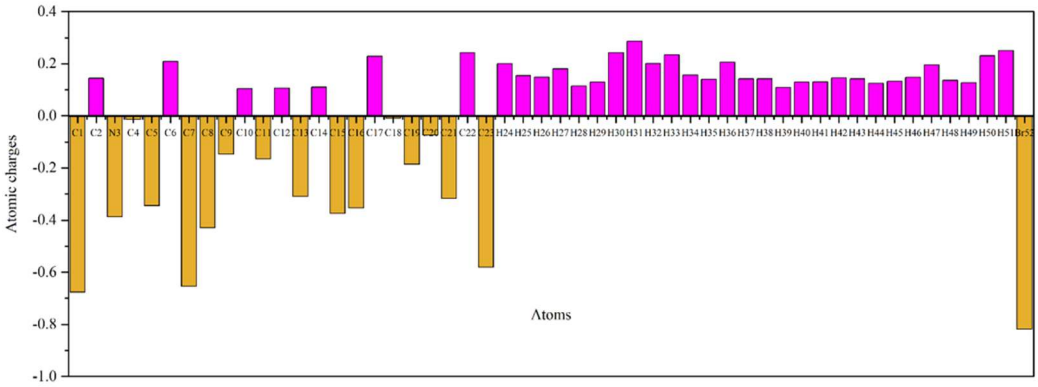

Fig. 11. Mulliken charge distributions of PB

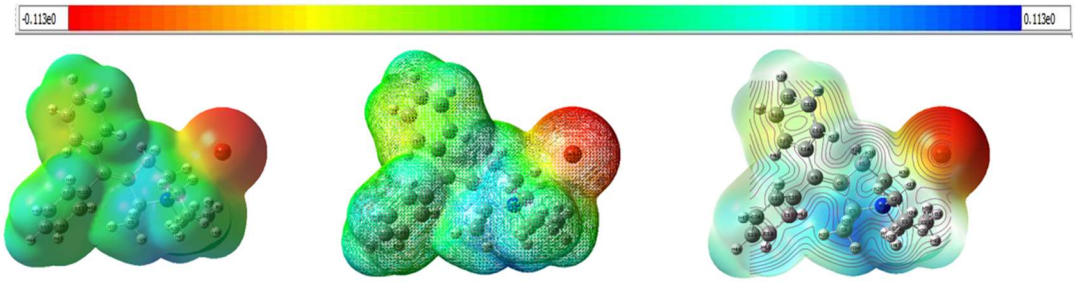

Fig. 12. The total electron density (left), mesh (middle) and the contour map (right) of MEP surface of PB

3.8 Topological Properties

3.8.1 ELF and LOL

The Electron Localization Function (ELF) and Localized Orbital Locator (LOL) analyses were performed to examine the electron density distribution and bonding characteristics in PB. These topological parameters help distinguish localized and delocalized electron regions within the molecular structure. The ELF and LOL results are visualized through color-filled maps, contour plots, and projected graphs, as shown in Figs. 13 and 14.

In PB, hydrogen atoms H31, H39, and H44 form covalent bonds with carbon atoms C5, C13, and C19, respectively. These regions are appeared in red, indicating high electron localization due to bonding interactions or lone pair concentrations. Similarly, the covalent nature of bonds between C9-C10 and C9-C16 is highlighted in red, emphasizing strong electron localization in these regions. Conversely, carbons C9, C10, C13, C16, and C19 in the diphenyl methylene structure, along with bromide ion (Br52), appear in blue in ELF maps, marking areas of electron delocalization and reduced electron localization. This suggests significant charge dispersal in these regions, indicative of π-electron delocalization and ionic interactions. In the LOL analysis, regions of delocalized electron population are enveloped in blue rings, including C9, C10, C13, C16, C19, and Br52, reaffirming their role in extended electron delocalization and molecular stability. In contrast, red rings around H31, H39, and H44 indicate localized electron density, further validating the ELF observations.

3.8.2 RDG and NCI

The Reduced Density Gradient (RDG) and Non-Covalent Interaction (NCI) analyses provide insights into weak interactions such as hydrogen bonding, van der Waals forces, and steric repulsions, which contribute to the stabilization of the molecular structure. The RDG scatter plot and NCI iso-surface map for PB are presented in Figs. 15 and 16, respectively. The RDG scatter plot displays three distinct regions, represented by blue, red, and green, corresponding to different types of non-covalent interactions. The blue region indicates hydrogen bonding, particularly between the methylene group of the methyl pyrrolidine ring and bromide ion, confirming strong electrostatic interactions. The red region highlights steric repulsions, marking regions where electron density clashes within the molecular framework. The green region represents van der Waals interactions, suggesting weak dispersion forces that contribute to overall molecular stability. In the NCI iso-surface map, red regions within the diphenyl methylene and methyl pyrrolidine ring structures signify steric repulsion, where overlapping electron clouds create destabilizing interactions. The green regions along molecular boundaries, particularly between methylene and methine groups, indicate van der Waals forces, which aid in molecular packing. Additionally, the blue region signifies a hydrogen bond interaction between the methylene group and bromide ion, reinforcing electrostatic stabilization within the structure.

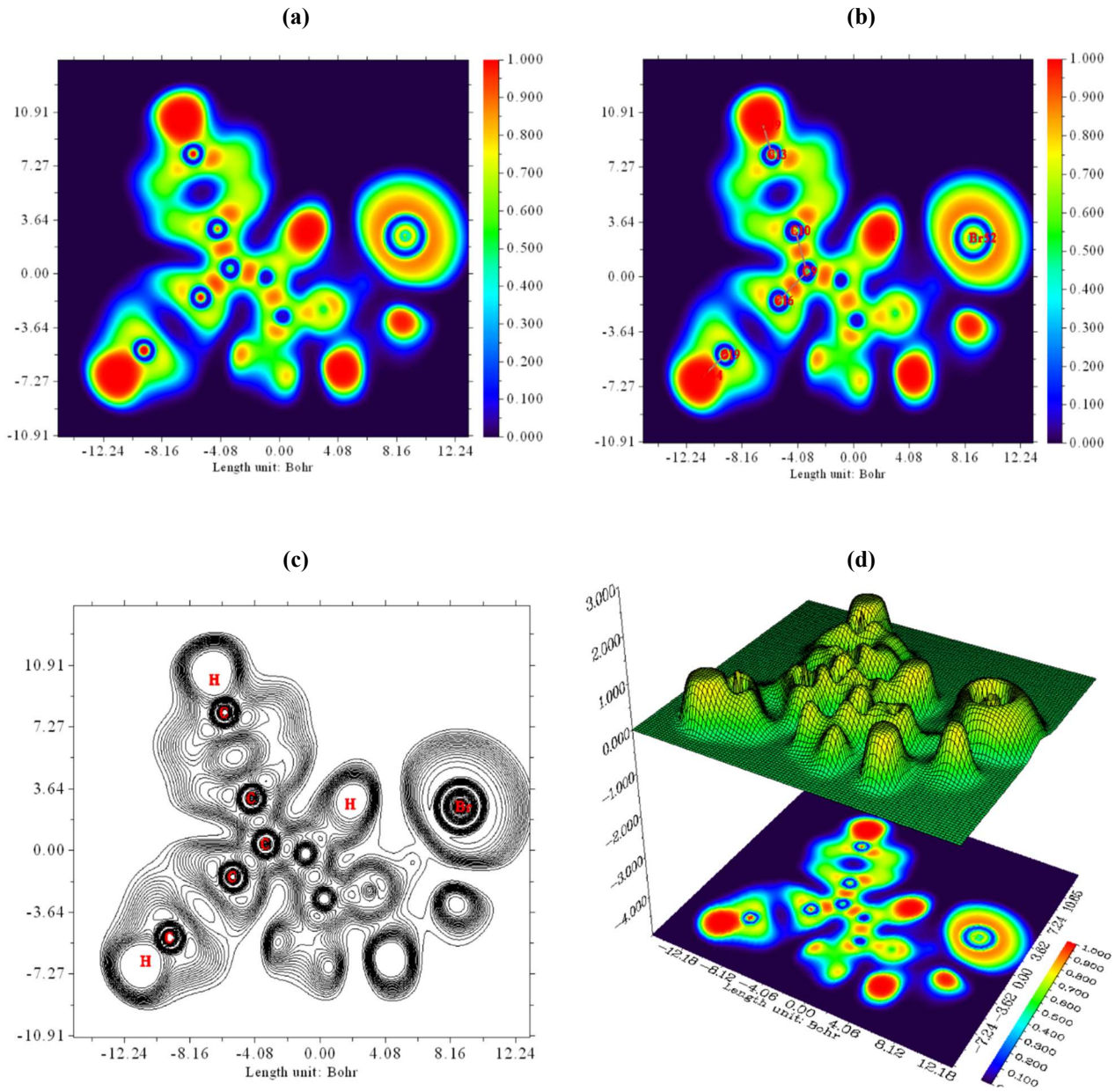

Fig. 13. (a) ELF diagram, (b) ELF diagram with numbering scheme, (c) contour map, and (d) ELF projection of PB

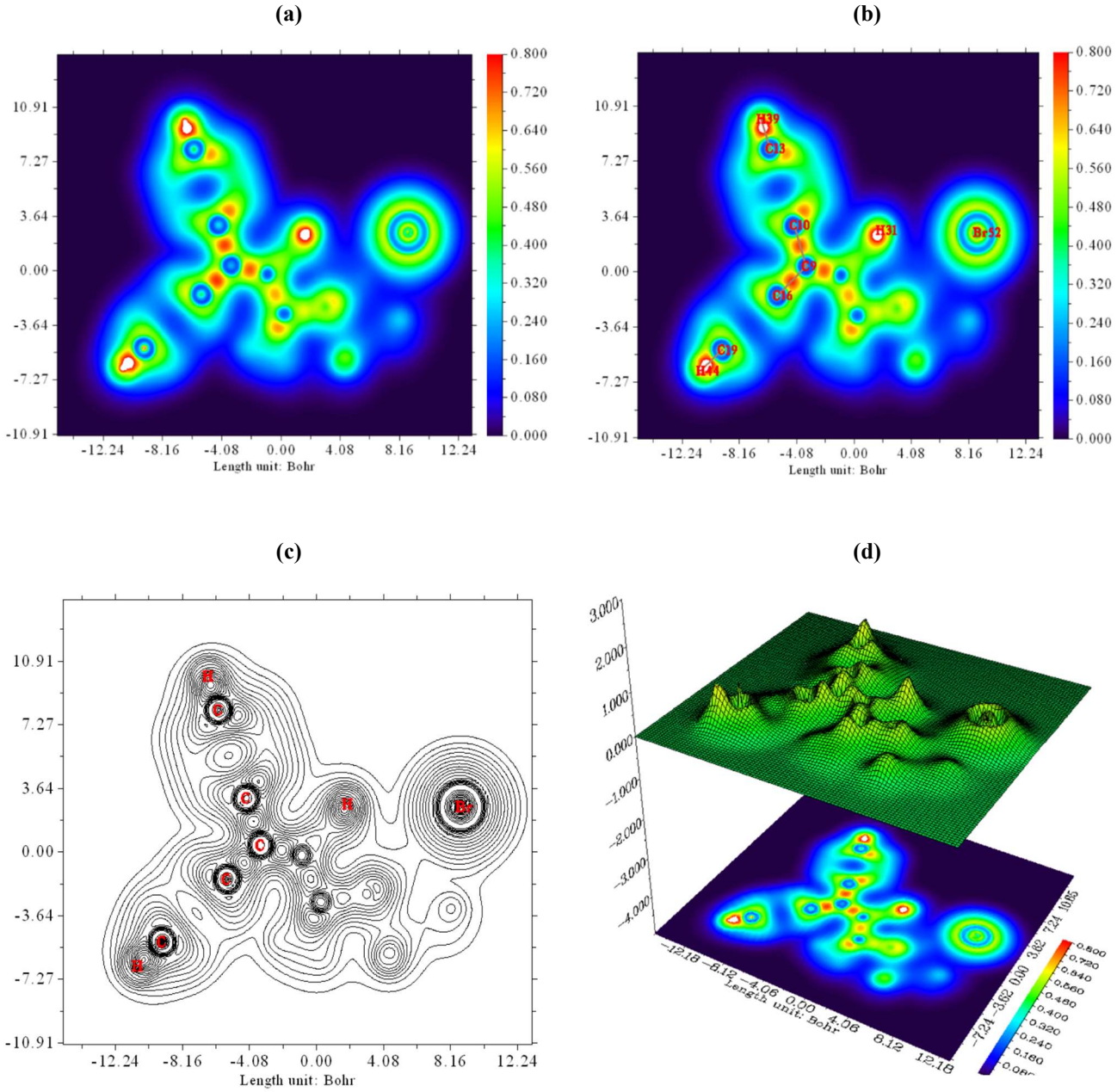

Fig. 14. (a) LOL diagram, (b) LOL diagram with numbering scheme, (c) contour map, and (d) LOL projection of PB

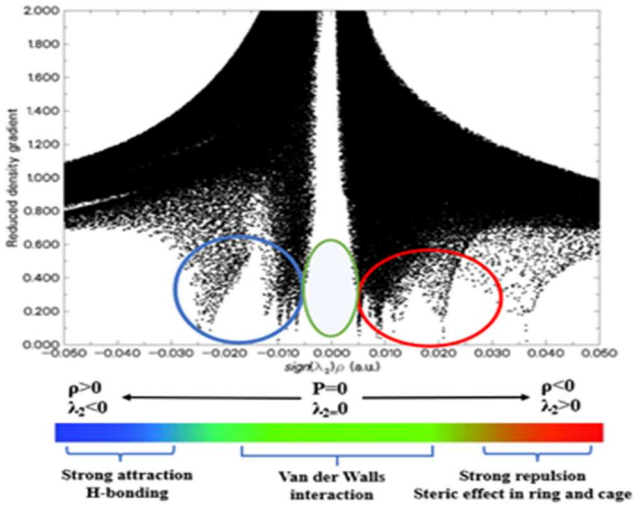

Fig. 15. RDG scatter plot of PB

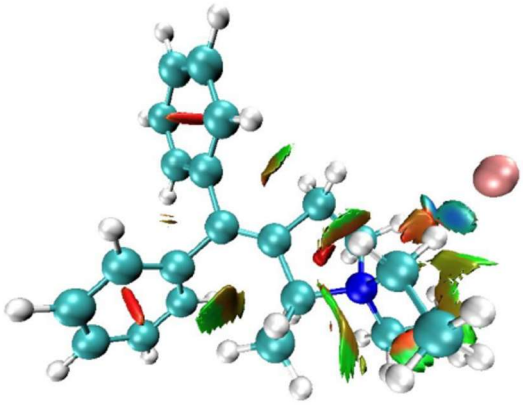

Fig. 16. NCI iso-surface map of PB

3.8.3 QTAIM

The Quantum Theory of Atoms in Molecules (QTAIM), developed by Bader, provides a rigorous framework for analyzing the topological properties of electron density to differentiate between covalent and non-covalent interactions. QTAIM identifies critical points in electron density that define molecular interactions, including bond critical points (BCPs) and ring critical points (RCPs). The analysis involves several key parameters, including electron density ρ(r), Laplacian of electron density $\nabla^2\rho(r)$, energy density H(r), Lagrangian kinetic energy G(r), and potential energy density V(r). These descriptors help characterize the nature and strength of bonding interactions. The eigenvalues of the Hessian matrix, along with ELF, LOL, ellipticity, and bond energy values, are listed in Table S5 (Supplementary Material).

In PB structure, 10 BCPs and 2 RCPs were identified. Among these, BCP74 and BCP84 indicate strong hydrogen bonding interactions, while BCP98 represents a moderate hydrogen bond interaction (H27… Br52). This H27 … Br52 interaction is particularly significant, as it defines an active region within the optimized molecular structure, contributing to its binding affinity with target receptors. The structural and electronic properties identified through QTAIM analysis strongly correlate with the biological activity of PB, demonstrating its functional role at both structural and electronic levels. The QTAIM molecular graph of PB is presented in Fig. 17, visually mapping its bonding interactions and electronic structure.

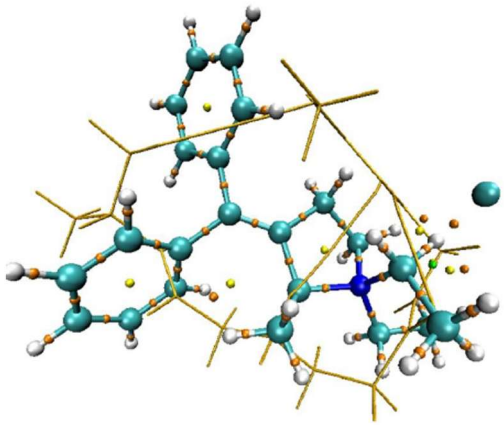

Fig. 17. QTAIM molecular graph of PB

3.9 Drug-Likeness and ADME

Drug-likeness refers to a set of properties that determine the potential of a chemical compound to be developed into a safe and effective drug. A compound's ability to be absorbed, distributed, metabolized, and excreted (ADME) plays a crucial role in its efficacy and safety. Additionally, minimal toxicity is essential to ensure its suitability for therapeutic use. The drug-likeness properties of PB are listed in Table S6 (supplementary material), were assessed using the SwissADME online tool based on Lipinski's rule of five (Lipinski et al., 2012). According to this rule, a drug-like compound should have an MlogP ≤ 5, a molecular weight ≤ 500, hydrogen bond donors ≤ 5, hydrogen bond acceptors ≤ 10, and a topological polar surface area (TPSA) ≤ 140 Å².

In this study, PB has a molecular weight of 386.37 g/mol, with no hydrogen bond donors or acceptors, an MlogP value of 1.39, and a TPSA of 0.00 Å², which influence its absorption, distribution, and permeability. Due to its low permeability in the gastrointestinal (GI) tract, PB may have limited oral bioavailability. Additionally, its inability to cross the blood-brain barrier (BBB) suggests it is unsuitable for central nervous system (CNS) related treatments but may still be effective for peripheral therapeutic applications. PB meets Lipinski's, Ghose's, Veber's, and Egan's criteria, indicating favorable oral bioavailability. However, it does not comply with Muegge's rule due to an XLOGP3 value exceeding 5 and a low number of heteroatoms (< 2). The bioavailability score of 0.55 suggests moderate oral absorption, though its poor solubility and limited GI absorption may restrict systemic exposure. Further experimental validation is needed to confirm these computational predictions and optimize its pharmacokinetic profile for clinical use.

3.10 Molecular Docking

In computational chemistry, molecular docking predicts the interaction between chemical structures and target proteins (Kalyan et al., 2024, Mohanapriya et al., 2024). The 3D structure of the human muscarinic receptor M2 (PDB ID: 5ZKC), a G-protein-coupled receptor with 421 amino acids, was retrieved from the Research Collaboratory for Structural Bioinformatics Protein Data Bank (RCSB PDB) with a resolution of 2.30 Å, confirmed using X-ray diffraction. The bound ligand (N-methyl scopolamine) and water molecules were removed, and the structure was formatted in PDB format. The molecular structure of PB was optimized without geometrical restrictions and formatted accordingly. Molecular docking simulations between PB and the target protein generated nine conformations, with the lowest binding energy conformation being the most stable. The 3D and 2D interaction plots of PB and the target protein are shown in Fig. 18 and detailed in Table 5. PB forms hydrophobic interactions with tyrosine (430, 426, 104, 403), aspartic acid (103), cysteine (429), serine (107), valine (111), alanine (194, 191), threonine (187, 190), tryptophan (400), phenylalanine (181, 195), and asparagine (404), with a binding energy of -8.6 kcal/mol. These results indicate that PB possesses strong anticholinergic properties by inhibiting the human muscarinic receptor M2, suggesting its potential as a therapeutic candidate for neurodegenerative diseases.

Table 5. Molecular docking studies of PB against 5KZC

Ligand	Protein	Binding energy (kcal/mol)	Hydrophobic interaction
PB	5KZC	-8.6	Tyrosine 430, 426, 104,403 Aspartic acid 103 Cysteine 429 Serine 107 Valine 111 Alanine 194, 191 Threonine 187, 190 Tryptophan 400 Phenylalanine 181, 195 Asparagine 404

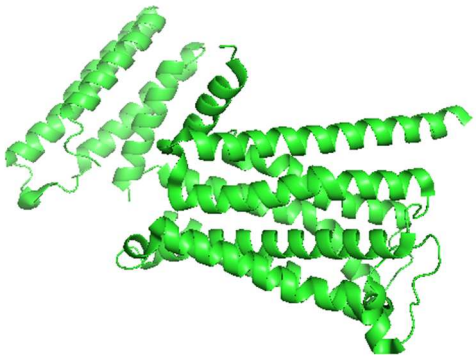

Fig. 18(a). Native structure of 5ZKC

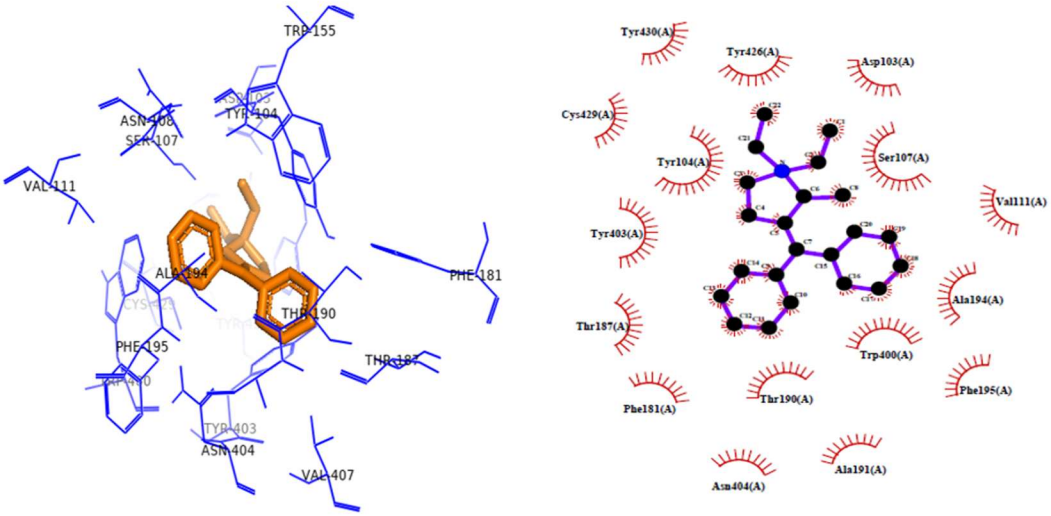

Fig. 18(b). The 3D PyMOL view (*left*) and 2D LigPlot+ view(*right*) of PB against 5ZKC

4. CONCLUSION

Prifinium bromide (PB), a quaternary ammonium compound, was analyzed for its structural, biological, topological, and spectroscopic properties. The N3-C7 and C6-C7 bonds were elongated due to electronic and steric effects in the pyrrolidinium ring, while hybridization effects caused deviations in bond lengths and angles, particularly in C2-H27 (longest), C11-H37 (shortest), and C1-C2-N3 (117.3°). A PES scan identified the most stable conformer at 130°, 240°, and 370° for N3-C22-C23-H51 and at 167° and 527° for C7-N3-C22-C23. The theoretical and experimental NMR data revealed deviations in chemical shifts, especially for methylene protons and carbons in the diethyl groups and pyrrolidinium ring, influenced by the quaternary nitrogen. Additionally, C10 and C16 showed deviations, likely due to resonance effects within the phenyl rings, while the bridge carbon (C9) exhibited significant electronic influence from both rings. Vibrational spectra identified key stretching and deformation modes for C-N, C-H, C-C, CH_2, and CH_3 groups of PB. Electronic spectra identified six transitions (482–382 nm), with the most intense absorption at 473 nm. An experimental peak at 379 nm correlated with calculated transitions at 382–388 nm. The FMO gap of 3.0501 eV suggests moderate stability and a feasible electronic excitation potential. NBO analysis confirmed strong classical bonding, with 98.335% Lewis and 1.665% non-Lewis electron density. Bromide-induced polarization was observed in LP(n) Br52 → σ*(C2-H27) and LP(n) Br52 → σ*(C4-H30). Mulliken charge analysis indicated electron density accumulation at the quaternary nitrogen (-0.38751 e) and strong electronegativity at bromide (-0.81746 e). Among the carbon atoms, C1, C7, and C23 carried the most negative charges, while H30, H31, H33, and H51 were highly polarized, as further supported by MEP surfaces. Topological analysis highlighted localized, delocalized, and weak interactions within PB, providing insights into its electronic environment. While PB meets Lipinski's, Ghose's, Veber's, and Egan's drug-likeness criteria, it violates Muegge's rule. Nevertheless, its bioavailability score of 0.55 suggests moderate oral absorption; however, poor solubility and low GI absorption may limit systemic exposure, necessitating further clinical validation. Additionally, molecular docking simulations confirmed PB's anticholinergic potential, with a binding affinity of -8.6 kcal/mol for the 5ZKC M2 muscarinic receptor, highlighting its promise as a therapeutic candidate for neurodegenerative disorders.

ACKNOWLEDGMENT

The authors acknowledge SAIF, St. Peter's Institute for Higher Education and Research, Chennai, for FT-IR and UV-Vis spectral measurements. They also thank IIT Madras, Chennai, for FT-Raman spectral measurements. Additionally, they acknowledge SCIF, SRM Institute of Science and Technology, Chennai, for NMR spectral measurements.

REFERENCES

Abu Nameh, E. 2013. Simple and validated spectrophotometric method for determination of prifinium bromide in pharmaceutical preparations. Australian Journal of Basic Applied Sciences, 7, 746–750.

Akshay Kalyan S., Kanagathara, N., Marchewka, M.K., Janczak, J., Senthilkumar, K. 2024. Structure, Spectroscopy, and Theoretical insights on Co-crystals of 2, 4-Diamino-6-Methyl-1, 3, 5-Triazine Bis (4-Aminobenzoic acid) Monohydrate as a promising anti-cancer agent. Physica B: Condensed Matter, 679, 415807.

Amro, A.N. 2019. Voltammetric determination of prifinium bromide in a pharmaceutical formulation. Journal of Taibah University for Science, 13, 1158–1162.

Arnold, W.A., Blum, A., Branyan, J., Bruton, T.A., Carignan, C.C., Cortopassi, G., Datta, S., DeWitt, J., Doherty, A.C., Halden, R.U. and Harari, H., 2023. Quaternary ammonium compounds: a chemical class of emerging concern. Environmental Science and Technology, 57(20), 7645–7665.

Becke, A.D. 1993. Density functional thermo chemistry–I: The effect of the exchange only gradient correlation. Journal of Chemical Physics, 98, 5648–5652.

DeLano, W.L. 2002. Pymol: an open-source molecular graphics tool. CCP4 Newsletter on Protein Crystallography, 40(1), 82–92.

Divya, P., Reeda, V.J., Selvaraj, S., Jothy, B. 2024. Theoretical spectroscopic electronic elucidation with polar and nonpolar solvents (IEFPCM model), molecular docking and molecular dynamic studies on bendiocarb-antiallergic drug agent. Journal of Molecular Liquids, 404, 124895.

Frisch, M.J. 2009. Gaussion 09W, Revision A. 02, Gaussion Inc. Walling ford, CT.

Hora, P.I., Pati, S.G., McNamara, P.J., Arnold, W.A. 2020. Increased use of quaternary ammonium compounds during the SARS-CoV-2 pandemic and beyond: considering environmental implications. Environmental Science and Technology Letters, 7, 622–631.

Humphrey, W., Dalke, A., Schulten, K. 1996. Visual Molecular Dynamics. Journal of Molecular Graphics, 14, 33–8.

Jeba Reeda, V., Divya, P., Ranchani, A.A.J., Manikandan, A., Alvi, S., Ali, R., Siddiqui, N., Haq, N., Muthu, S., Butcher, R., Javed, S. 2025. Comprehensive analysis of 2, 5-dimethyl-1-(naphthalen-1-yl)-1H-pyrrole: X-ray crystal structure, spectral, computational, molecular properties, docking studies, molecular dynamics, and MMPBSA. Journal of Molecular Structure, 1321, 140062.

Kohn, W., Sham, L.J. 1965. Self-consistent equations including exchange and correlation effects. Physical Review, 140, A1133–A1138.

Kumada, S., Kozatani, J., Seki, M. 1970. Studies on the ratio of equipotent oral and subcutaneous doses in man of prifinium bromide, new synthetic spasmolytic. Arzneimittel-Forschung, 20, 237–240.

Lataifeh, A., Wedian, F. 2014. bivariate calibration method vs. hplc and derivative spectroscopy for simultaneous determination of binary drugs in pharmaceutical formulations: a study on prifinium bromide/paracetamol and amoxicillin/potassium clavulanate. Analytical Chemistry Letters, 4, 240–254.

Lee, C., Yang, W., Parr, R.G. 1988. Development of the Colle-Salvetti correlation-energy formula into a functional of the electron density. Physical Review B, 37, 785–789.

Lipinski, C.A. Lombardo, F., Dominy, B.W., Feeney, P.J. 2012. Experimental and computational approaches to estimate solubility and permeability in drug discovery and development settings. Advanced Drug Delivery Reviews, 64, 4–7.

Lu, T., Chen, F. 2012. Multiwfn: a multifunctional wavefunction analyzer. Journal of Computational Chemistry, 33, 580–592.

Moayyedi, P., Andrews, C.N., MacQueen, G., Korownyk, C., Marsiglio, M., Graff, L., Kvern, B., Lazarescu, A., Liu, L., Paterson, W.G., Sidani, S. 2019. Canadian association of gastroenterology clinical practice guideline for the management of irritable bowel syndrome (IBS). Journal of the Canadian Association of Gastroenterology, 2, 6–29.

Mohanapriya, E., Elangovan, S., Kanagathara, N., Marchewka, M.K., Janczak, J., Revathi, P. 2024. Density functional theory calculations, structural and spectroscopic characterization, and solvent-dependent HOMO-LUMO studies of 2-nitro-4-methylanilinium benzenesulfonate. Journal of Molecular Structure, 1317, 139147.

Moriyoshi, M., Maruyama, Y., Iseki, K., Nakao, T. 1999. Induction of parturition in bitches with minimal side effects by two injections of a low dose of fenprostalene, a prostaglandin F22α analogue, and pretreatment with prifinium bromide. Journal of Veterinary Medical Science, 61, 781–786.

Morris, G.M., Huey, R., Lindstrom, W., Sanner, M.F., Belew, R.K., Goodsell, D.S., Olson, A.J. 2009. AutoDock4 and AutoDockTools4: Automated docking with selective receptor flexibility. Journal of Computational Chemistry, 30, 2785–2791.

Musumarra, G., Scarlata, G., Romano, G., Cappello, G., Clementi, S., Giulietti, G. 1987. Qualitative organic analysis. Part 2. Identification of drugs by principal components analysis of standardized TLC data in four eluent systems and of retention indices on SE 30. Journal of Analytical Toxicology, 11, 154–163.

Petersilka, M., Gossman, U.J., Gross, E.K.U. 1966. Excitation energies from timedependent density-functional theory. Physical Review Letters, 76, 1212–1215.

Piai, G., Mazzacca, G. 1979. Prifinium bromide in the treatment of the irritable colon syndrome. Gastroenterology, 77, 500–502.

Rajkumar, P., Selvaraj, S., Suganya, R., Velmurugan, D., Gunasekaran, S., Kumaresan, S. 2018. Vibrational and electronic spectral analysis of thymol an isomer of carvacrol isolated from Trachyspermum ammi seed: a combined experimental and theoretical study. Chemical Data Collections, 15, 10–31.

Ram Kumar, A., Ilavarasan, L., Sheeja Mol, G., Selvaraj, S., Azam, M., Jayaprakash, P., Kesavan, M., Alam, M., Dhanalakshmi, J., Al-Resayes, S.I., Ravi, A. 2023. Spectroscopic (FT-IR, FT-Raman, UV-Vis and NMR) and computational (DFT, MESP, NBO, NCI, LOL, ELF, RDG and QTAIM) profiling of 5-chloro-2-hydroxy-3-methoxybenzaldehyde: A promising antitumor agent. Journal of Molecular Structure, 1298, 136974.

Ram Kumar, A., Selvaraj, S., Azam, M., Sheeja Mol, G.P.,

Kanagathara, N., Alam, M., Jayaprakash, P. 2023. Spectroscopic, biological, and topological insights on lemonol as a potential anticancer agent. ACS Omega, 8, 31548–31566.

Ram Kumar, A., Selvaraj, S., Kanagathara, N. 2024. Spectroscopic, structural and molecular docking studies on N, N-Dimethyl-2-[6-methyl-2-(4-methylphenyl) Imidazo [1, 2-a] pyridin-3-yl] Acetamide. Physical Chemistry Research, 12, 95–107.

Ram Kumar, A., Selvaraj, S., Sheeja Mol, G., Selvaraj, M., Ilavarasan, L., Pandey, S.K., Jayaprakash, P., Awasthi, S., Albormani, O., Ravi, A. 2023. Synthesis, solvent-solute interactions (polar and nonpolar), spectroscopic insights, topological aspects, Fukui functions, molecular docking, ADME, and donor-acceptor investigations of 2-(trifluoromethyl) benzimidazole: A promising candidate for antitumor pharmacotherapy. Journal of Molecular Liquids, 393, 123661.

Rama, I., Subashini, A., Nadhiya, M., Ragavendran, V., Kanagathara, N. and Ahamed, A.A. 2023. Synthesis, spectral characterization, SC-XRD, Hirshfeld, DFT and in silico antidiabetic activity of novel imine (E)-N-(2-nitro benzylidene) naphthalene-1-amine, a newly synthesized imine: A theoretical and experimental evaluation. Journal of Molecular Structure, 1292, 136084.

Rathika, A., Reeda, V.J., Divya, P. 2024. Synthesis, spectroscopic analysis (FT-IR, FT-Raman, UV, NMR), non-covalent interactions (RDG, IGM) and dynamic simulation on Bis (8-hydroxy quinoline) salicylate salicylic acid. Journal of Molecular Structure, 1310, 138231.

Runge, E., Gross, E.K.U. 1984. Density functional theory for time-dependent systems. Physical Review Letters, 52, 997.

Sasa, S.I., Jalal, I.M., Khalil, H.S. 1988. Determination of prifinium bromide in six pharmaceutical formulations by reverse-phase HPLC. Journal of Liquid Chromatography, 11, 447–462.

Sasaki, D., Munakata, A., Saitoh, Y., Yoshida, Y. 1981. Antispasmodic effect of prifinium bromide on the proximal and distal colon in patients with diverticular disease. Gastroenterologia Japonica, 16, 344–349.

Selvaraj, S., Rajkumar, P., Thirunavukkarasu, K., Gunasekaran, S., Kumaresan, S. 2018. Vibrational (FT-IR and FT-Raman), electronic (UV–vis) and quantum chemical investigations on pyrogallol: A study on benzenetriol dimers. Vibrational Spectroscopy, 95, 16–22.

Selvaraj, S., Ram Kumar, A., Ahilan, T., Kesavan, M., Gunasekaran, S., Kumaresan, S. 2022. Multi spectroscopic and computational investigations on the electronic structure of oxyclozanide. Journal of Indian Chemical Society, 99, 100676.

Silverstein, R.M., Bassler, G.C. 1962. Spectrometric identification of organic compounds. Journal of Chemical Education, 39, 546.

Terai, T., Deguchi, Y., Ohtsuka, M., Kumada, S. 1991. Effects of the anticholinergic drug prifinium bromide on urinary bladder contractions in rat in vivo and in guinea-pig in vitro. Arzneimittel-Forschung, 41, 417–420.

Thirunavukkarasu, M., Balaj, G., Shanthi, D., Prabakaran, P., Irfan, A., Muthu, S. 2022. Experimental spectroscopic investigations, solute-solvent interactions, topological analysis and biological evaluations of N-(9-Fluorenylmethoxycarbonyloxy) succinimide: An effective agent in anti-breast cancer activity. Journal of Molecular Liquids, 362, 119756.

Tokuma, Y., Tamura, Y., Noguchi, H. 1982. High-performance liquid chromatographic determination of prifinium quaternary ammonium ion in human serum and urine. Journal of Chromatography B: Biomedical Sciences and Applications, 231, 129–136.

Vereshchagin, A.N., Frolov, N.A., Egorova, K.S., Seitkalieva, M.M. and Ananikov, V.P. 2021. Quaternary ammonium compounds and ionic liquids as biocides: From simple antiseptics to tunable antimicrobials. International Journal of Molecular Sciences, 22, 6793.

Vijayalakshmi, V., Kanagathara, N., Jan, J., Marchewka, M.K., Mohammad, A., Senthilkumar, K. 2024. Structural, spectroscopic and second harmonic generation evaluation of 1, 2, 4-triazolinium tartrate-tartaric acid as a promising nonlinear optical material. Optical Materials, 147, 11469.

Wallace, A.C., Laskowski, R.A., Thornton, J.M. 1995. LIGPLOT: a program to generate schematic diagrams of protein–ligand interactions. Protein Engineering Design and Selection 8, 127–134.

Zhang, C., Cui, F., Zeng, G.M., Jiang, M., Yang, Z.Z., Yu, Z.G., Shen, L.Q. 2015. Quaternary ammonium compounds: A review on occurrence, fate and toxicity in the environment. Science of the Total Environment, 518, 352–362.

Zhurko, G.A., Zhurko, D.A. 2009. Chemcraft Program Version 1.6 (Build 315).

Table S1. Calculated conformational energies for possible conformers of PB

No. Scanning of Steps	$\phi_1(N_3\text{-}C_{22}\text{-}C_{23}\text{-}H_{51})$			$\phi_2(C_7\text{-}N_3\text{-}C_{22}\text{-}C_{23})$		
	Scan Coordinate (degree)	Energy		Scan Coordinate (degree)	Energy	
		Hartree	kcal/mol		Hartree	kcal/mol
1	50.28012634	-3481.544073	-2184702.36	167.3155845	-3481.546317	-2184703.76
2	60.28012634	-3481.543461	-2184701.97	177.3155845	-3481.54612	-2184703.64
3	70.28012634	-3481.543084	-2184701.74	187.3155845	-3481.544364	-2184702.54
4	80.28012634	-3481.543664	-2184702.10	197.3155845	-3481.541942	-2184701.02
5	90.28012634	-3481.54471	-2184702.76	207.3155845	-+3481.537921	-2184698.50
6	100.2801263	-3481.545551	-2184703.28	217.3155845	-3481.533035	-2184695.43
7	110.2801263	-3481.546088	-2184703.62	227.3155845	-3481.528753	-2184692.74
8	120.2801263	-3481.546322	-2184703.77	237.3155845	-3481.526346	-2184691.23
9	130.2801263	-3481.546357	-2184703.79	247.3155845	-3481.5262	-2184691.14
10	140.2801263	-3481.546259	-2184703.73	257.3155845	-3481.527727	-2184692.10
11	150.2801263	-3481.545951	-2184703.54	267.3155845	-3481.530462	-2184693.82
12	160.2801263	-3481.545251	-2184703.10	277.3155845	-3481.533988	-2184696.03
13	170.2801263	-3481.544196	-2184702.43	287.3155845	-3481.536846	-2184697.82
14	180.2801263	-3481.543472	-2184701.98	297.3155845	-3481.538853	-2184699.08
15	190.2801263	-3481.543075	-2184701.73	307.3155845	-3481.539782	-2184699.66
16	200.2801263	-3481.543849	-2184702.22	317.3155845	-3481.539021	-2184699.19
17	210.2801263	-3481.544882	-2184702.86	327.3155845	-3481.536893	-2184697.85
18	220.2801263	-3481.545679	-2184703.36	337.3155845	-3481.533916	-2184695.98
19	230.2801263	-3481.546151	-2184703.66	347.3155845	-3481.531736	-2184694.62
20	240.2801263	-3481.546339	-2184703.78	357.3155845	-3481.531512	-2184694.47
21	250.2801263	-3481.54635	-2184703.79	367.3155845	-3481.53299	-2184695.40
22	260.2801263	-3481.546226	-2184703.71	377.3155845	-3481.535735	-2184697.12
23	270.2801263	-3481.545865	-2184703.48	387.3155845	-3481.539382	-2184699.41
24	280.2801263	-3481.54509	-2184702.99	397.3155845	-3481.542365	-2184701.28
25	290.2801263	-3481.544071	-2184702.36	407.3155845	-3481.543736	-2184702.15
26	300.2801263	-3481.543422	-2184701.95	417.3155845	-3481.543762	-2184702.16
27	310.2801263	-3481.543074	-2184701.73	427.3155845	-3481.542741	-2184701.52
28	320.2801263	-3481.543623	-2184702.07	437.3155845	-3481.540928	-2184700.38
29	330.2801263	-3481.544702	-2184702.75	447.3155845	-3481.538633	-2184698.94
30	340.2801263	-3481.545577	-2184703.30	457.3155845	-3481.536326	-2184697.50
31	350.2801263	-3481.546119	-2184703.64	467.3155845	-3481.535179	-2184696.78
32	360.2801263	-3481.546335	-2184703.78	477.3155845	-3481.535947	-2184697.26
33	370.2801263	-3481.54635	-2184703.79	487.3155845	-3481.538104	-2184698.61
34	380.2801263	-3481.546217	-2184703.70	497.3155845	-3481.540896	-2184700.36
35	390.2801263	-3481.545827	-2184703.46	507.3155845	-3481.543607	-2184702.06
36	400.2801263	-3481.545016	-2184702.95	517.3155845	-3481.545553	-2184703.29
37	410.2801263	-3481.544073	-2184702.36	27.3155845	-3481.546317	-2184703.76

Table S2. Experimental and theoretical wave numbers along with vibrational assignments of PB

Serial No.	Experimental wavenumbers (cm^{-1})		Theoretical wavenumbers (cm^{-1})				Vibrational assignments
	FT-IR	FT-Raman	Unscaled	Scaled	I_{IR}	I_{Raman}	
1	-	-	3210	3085	9.42	332.73	υ CH
2	-	-	3208	3083	15.79	348.54	υ CH
3	-	-	3203	3078	24.80	55.07	υ CH
4	-	-	3198	3073	20.32	45.14	υ CH
5	-	-	3196	3071	12.44	70.36	υ CH
6	-	-	3191	3067	8.53	94.35	υ CH
7	-	-	3188	3064	0.67	113.57	υ CH
8	-	-	3183	3059	0.07	79.24	υ CH
9	-	-	3180	3056	1.87	34.81	υ CH
10	-	-	3176	3052	5.12	24.29	υ CH
11	-	3046	3169	3045	2.97	50.71	υ CH, υ_{as} CH_3
12	3032	-	3158	3035	13.86	15.10	υ CH, υ_{as} CH_2
13	-	-	3149	3026	10.37	12.45	υ_{as} CH_2 in CH_3
14	-	-	3145	3022	20.19	60.85	υ_{as} CH_3, υ CH in CH_2
15	-	-	3139	3017	6.41	43.81	υ_{as} CH_3, υ_{as} CH_2
16	-	-	3131	3009	3.90	75.18	υ_{as} CH_2
17	-	-	3129	3007	17.55	53.04	υ_{as} CH_2 in CH_3
18	-	-	3123	3001	2.70	76.70	υ_{as} CH_3, υ_{as} CH_2
19	-	2990	3120	2998	11.65	77.01	υ_{as} CH_2
20	-	-	3094	2973	43.74	103.67	υ_{as} CH_2
21	-	-	3076	2956	29.04	166.08	υ_{s} CH_2
22	2953	-	3072	2952	3.38	140.33	υ_{s} CH_2
23	-	-	3071	2951	28.49	152.52	υ_{s} CH_3
24	-	-	3063	2944	7.88	103.32	υ_{s} CH_3
25	-	2942	3060	2941	18.20	204.29	υ_{s} CH_3
26	-	-	3046	2927	5.93	58.47	υ CH
27	-	-	2986	2870	602.22	619.35	υ_{s} CH_2
28	-	-	2948	2833	166.95	126.33	υ_{s} CH_2
29	1688, 1611	1656	1683	1617	2.16	670.42	υ CC
30	1585	1596	1647	1583	3.22	162.48	υ CC
31	-	-	1644	1580	3.08	153.37	υ CC
32	-	-	1621	1558	1.16	18.51	υ CC
33	1511	-	1620	1557	1.86	12.09	υ CC, β CH
34	1477	-	1533	1473	18.85	5.28	υ CC, χ CH_2, δ_{as} CH_3
35	-	-	1528	1468	7.30	13.77	β CH, χ CH_2, δ_{as} CH_3
36	-	-	1527	1467	6.74	3.22	χ CH_2, δ_{as} CH_3
37	-	-	1526	1466	5.91	0.84	β CH
38	-	-	1519	1460	6.62	5.49	χ CH_2, δ_{as} CH_3
39	-	-	1512	1453	2.77	3.13	χ CH_2, δ_{as} CH_3
40	-	-	1510	1451	19.11	9.90	χ CH_2, δ_{as} CH_3
41	-	1441	1504	1445	5.46	10.91	χ CH_2, δ_{as} CH_3
42	-	-	1497	1439	17.95	3.29	χ CH_2, δ_{as} CH_3
43	-	-	1493	1435	1.93	1.76	χ CH_2, δ_{as} CH_3
44	-	-	1491	1433	5.62	6.84	χ CH_2, δ_{as} CH_3
45	-	-	1487	1429	13.42	17.31	χ CH_2, δ_{as} CH_3
46	1415	-	1477	1419	7.23	2.87	β CH
47	-	-	1475	1417	3.08	2.36	β CH
48	-	-	1466	1409	3.74	1.33	δ_{s} CH_3, ω CH_2
49	-	-	1446	1390	7.74	6.24	δ_{s} CH_3, ω CH_2
50	-	-	1429	1373	17.79	2.58	δ_{s} CH_3, ω CH_2
51	-	-	1425	1369	5.56	1.90	δ_{s} CH_3, β CH

52	-	-	1415	1360	2.19	1.49	δ_s CH_3, ω CH_2, β CH
53	-	-	1405	1350	13.34	2.34	δ_s CH_3, ω CH_2
54	1335	-	1378	1324	4.59	0.54	δ_s CH_3, τ CH_2, β CH
55	-	-	1370	1317	0.83	2.95	τ CH_2
56	-	-	1360	1307	1.19	1.40	β CH
57	-	1301	1356	1303	1.04	1.07	β CH
58	-	-	1343	1291	0.44	12.31	β CH, τ CH_2
59	1286	-	1337	1285	8.27	34.83	β CH, τ CH_2, υ CN
60	-	-	1329	1277	1.94	7.95	β CH, τ CH_2, υ CN
61	-	-	1324	1272	1.00	4.23	β CH, τ CH_2
62	-	-	1315	1264	19.14	5.43	β CH, τ CH_2
63	-	-	1299	1248	5.10	66.96	β CH, υ CC
64	1235	-	1275	1225	10.46	28.22	β CH, ρ CH_2, υ CN
65	-	1177	1241	1193	7.86	21.51	τ CH_2
66	-	1161	1208	1161	6.01	6.02	β CH
67	-	-	1206	1159	2.21	7.54	β CH, δ_{as} CH_3
68	-	-	1203	1156	1.02	9.68	β CH
69	-	-	1197	1150	1.13	67.97	β CH, τ CH_2
70	-	-	1192	1146	2.02	6.96	δ_{as} CH_3, ρ CH_2
71	-	-	1185	1139	0.05	6.02	β CH
72	1138	-	1184	1138	0.04	3.41	β CH
73	-	-	1180	1134	4.44	5.84	δ_{as} CH_3, ρ CH_2
74	1096	-	1136	1092	7.55	20.88	δ_{as} CH_3, τ CH_2
75	-	-	1123	1079	0.87	7.98	δ_{as} CH_3, τ CH_2
76	-	-	1111	1068	6.64	2.05	δ_{as} CH_3, β CH
77	-	-	1106	1063	6.00	0.63	β CH
78	-	-	1104	1061	9.49	2.58	δ_{as} CH_3, β CH
79	1051	-	1096	1053	10.08	3.98	δ_{as} CH_3, β CH, τ CH_2
80	-	1027	1066	1024	20.24	12.49	δ_{as} CH_3, β CH, ρ CH_2
81	-	-	1053	1012	8.49	6.90	β CH
82	-	-	1050	1009	0.38	42.01	β CH
83	-	-	1047	1006	14.99	4.50	δ_s CH_3, ρ CH_2, β CH
84	-	-	1080	1038	2.68	4.08	ω CH_2
85	-	998	1022	982	16.93	8.20	δ_{as} CH_3, ρ CH_2, γ CH
86	954	-	1014	974	0.93	39.34	δ_{as} CH_3, γ CH
87	-	-	1013.81	974	1.16	50.16	γ CH
88	-	-	1013.25	973	12.12	17.56	δ_{as} CH_3, ω CH_2
89	-	-	1007	968	0.08	2.51	γ CH
90	-	-	1006	967	1.05	0.30	γ CH
91	-	-	989	950	0.34	0.58	γ CH
92	-	-	987	949	0.33	0.69	γ CH
93	-	-	956	919	3.59	8.90	γ CH, δ_{as} CH_3, ρ CH_2
94	-	-	946	909	2.94	3.51	γ CH, δ_{as} CH_3, ω CH_2
95	-	-	941	904	1.62	0.59	γ CH, δ_{as} CH_3
96	-	-	935	899	6.99	1.30	γ CH, ρ CH_2
97	-	-	911	875	1.84	1.87	γ CH
98	-	-	881	847	1.06	12.71	γ CH, δ_{as} CH_3, ρ CH_2
99	849	-	875	841	0.77	4.56	γ CH, δ_{as} CH_3, ρ CH_2
100	-	-	863	829	0.14	3.84	γ CH
101	-	-	859	825	0.55	2.57	γ CH
102	804	-	853	820	2.50	1.76	δ_{as} CH_3, ρ CH_2
103	-	-	809	777	16.22	3.61	δ_{as} CH_3, ρ CH_2
104	-	-	790	759	8.58	2.19	δ_{as} CH_3, ρ CH_2
105	-	744	781	750	31.58	4.58	γ CH
106	733	-	770	740	40.57	2.09	γ CH, ρ CH_2
107	-	-	716	688	48.26	1.32	ρ CH_2

108	-	-	711.9	684	33.34	0.93	ρ CH_2
109	-	-	711.44	684	11.05	5.00	ρ CH_2, δ_{as} CH_3
110	663	-	696	669	1.08	2.24	δ_{as} CH_3, τ CH_2
111	-	-	675	649	5.82	2.57	δ_{as} CH_3,
112	-		643	618	3.00	2.81	ρ CH_2
113	-	615	642	617	6.44	2.87	ρ CH_2
114	-	-	630	605	0.30	7.22	ρ CH_2
115	-	-	626	602	0.73	2.51	ρ CH_2, δ_{as} CH_3
116	557	-	607	583	1.26	0.45	δ_{as} CH_3
117	-	-	550	528	3.90	9.73	δ_{as} CH_3, ρ CH_2
118	-	-	530	509	3.14	4.24	δ_{as} CH_3, ρ CH_2
119	-	-	500	481	3.59	2.20	δ_{as} CH_3
120	-	-	479	460	2.29	0.81	δ_{as} CH_3, ρ CH_2
121	-	-	441	424	1.70	1.82	ρ CH_2
122	-	-	420	404	5.36	3.31	ρ CH_2, δ_s CH_3, β CN
123	-	-	416	400	0.82	3.46	ρ CH_2
124	-	-	414	398	0.06	3.32	ρ CH_2
125	-	-	373	358	2.33	3.92	ρ CH_2, γ CH, δ_{as} CH_3
126	-	-	348	334	1.59	1.28	δ_{as} CH_3, ρ CH_2
127	-	-	344	331	0.66	0.16	δ_{as} CH_3, ρ CH_2
128	-	-	314	302	0.52	0.47	δ_{as} CH_3, ρ CH_2
129	-	-	306	294	0.34	0.66	ρ CH_2, δ_s CH_3
130	-	-	294	283	0.02	1.25	δ_{as} CH_3
131	-	-	274	263	0.44	3.15	δ_{as} CH_3, ρ CH_2
132	-	-	252	242	0.65	1.18	δ_{as} CH_3, ρ CH_2
133	-	-	241	232	4.09	6.09	δ_{as} CH_3, ρ CH_2
134	-	-	237	228	0.04	1.54	δ_{as} CH_3, ρ CH_2
135	-	-	227	218	4.13	1.02	δ_{as} CH_3, ρ CH_2
136	-	-	204	196	0.58	0.81	δ_{as} CH_3, ρ CH_2
137	-	-	197	189	1.84	1.37	δ_{as} CH_3, ρ CH_2
138	-	-	174	167	0.23	0.48	δ_{as} CH_3
139	-	-	167	160	0.13	0.81	δ_{as} CH_3, ρ CH_2
140	-	-	124	119	13.20	1.13	δ_{as} CH_3
141	-	-	118	113	3.91	0.77	δ_{as} CH_3
142	-	-	99	95	10.50	0.99	δ_{as} CH_3, ρ CH_2 υ Br
143	-	-	77	74	0.38	2.88	δ_{as} CH_3
144	-	-	68	65	1.13	1.93	δ_{as} CH_3
145	-	-	59	57	0.58	3.48	γ CH
146	-	-	52	50	0.37	13.61	γ CH
147	-	-	39	37	1.00	0.65	δ_s CH_3, γ CH, ρ CH_2, υ Br
148	-	-	32	31	1.92	2.57	δ_s CH_3, γ CH, ρ CH_2, υ Br
149	-	-	28	27	3.55	0.55	δ_{as} CH_3, γ CH, υ Br
150	-	-	17	16	4.83	0.48	δ_s CH_3, γ CH, ρ CH_2, υ Br

υ_s –symmetric stretching;
υ_{as} –asymmetric stretching;
δ–bending / deformation;
β–in-plane bending;
γ–out-of-plane bending;
χ–scissoring;
ω–wagging;
τ–twist;
ρ–rocking,
Scaling factor 0.96 for all vibrations

Table S3. The FMO and other characteristics of PB

Parameters	Formula	Values
E_{HOMO} (eV)	-	-8.0363
E_{LUMO} (eV)	-	-4.9862
$E_{HOMO\text{-}LUMO}$ gap (eV)	-	3.0501
Ionization potential (I) (eV)	$-E_{HOMO}$	8.0363
Electron affinity (A) (eV)	$-E_{LUMO}$	4.9862
Electronegativity (χ) (eV)	(I+A)/2	6.5112
Chemical potential (μ) (eV)	-χ	-6.5112
Chemical hardness (η) (eV)	(I-A)/2	1.5250
Chemical softness (s) (eV^{-1})	1/2η	0.3278
Global Electrophilicity (ω) (eV)	$\mu^2/2\eta$	13.9002
Maximum electron charge (ΔNmax)	−(μ/η)	4.2696

Table S4. Mulliken charge distributions of PB

Atoms	Charges (e)	Atoms	Charges €
C_1	-0.67562	H_{27}	0.181214
C_2	0.14463	H_{28}	0.115292
N_3	-0.38751	H_{29}	0.129357
C_4	-0.01355	H_{30}	0.242657
C_5	-0.34429	H_{31}	0.285895
C_6	0.209706	H_{32}	0.201681
C_7	-0.65352	H_{33}	0.233862
C_8	-0.42937	H_{34}	0.157161
C_9	-0.14639	H_{35}	0.141562
C_{10}	0.104566	H_{36}	0.205206
C_{11}	-0.16445	H_{37}	0.142237
C_{12}	0.106473	H_{38}	0.141777
C_{13}	-0.3085	H_{39}	0.108996
C_{14}	0.110264	H_{40}	0.129497
C_{15}	-0.37343	H_{41}	0.131246
C_{16}	-0.35386	H_{42}	0.145016
C_{17}	0.228563	H_{43}	0.141942
C_{18}	-0.0091	H_{44}	0.125554
C_{19}	-0.18467	H_{45}	0.132578
C_{20}	-0.07338	H_{46}	0.148154
C_{21}	-0.31666	H_{47}	0.195552
C_{22}	0.242677	H_{48}	0.136286
C_{23}	-0.58077	H_{49}	0.126786
H_{24}	0.200514	H_{50}	0.230693
H_{25}	0.154715	H_{51}	0.250806
H_{26}	0.149396	Br_{52}	-0.81746

Table S5. Quantum theory of atoms in molecules bond critical points (BCP), ring critical points (RCP) and other parameters of PB

Interactions	ρ(r) a.u	∇^2 ρ(r) a.u	H(r) a.u	G(r) a.u	V (r) a.u	λ1 a.u	λ2 a.u	λ3 a.u	ELF	LOL	Ellipticity	Binding energy (kJ/mol)
RCP1 RCP65 Type (3,+1)	0.0209	0.1292	0.0054	0.0268	-0.0213	-0.0126	0.0674	0.0744	0.0281	0.1455	-1.187	-27.961
RCP2 RCP111 Type (3,+1)	0.0209	0.1292	0.0055	0.0268	-0.0213	-0.0125	0.0671	0.0746	0.0281	0.1452	-1.187	-27.961
BCP1 BCP66 Type (3,-1) C_{35}…C_{16}	0.0099	0.0358	0.0014	0.0075	-0.0060	-0.0063	-0.0045	0.0466	0.0302	0.1501	0.387	-7.876
BCP2 BCP72 Type (3,+1)	0.0091	0.0335	0.00007	0.0076	-0.0069	-0.0041	0.0058	0.0317	0.0218	0.1302	-1.706	-9.747
BCP3 BCP74 Type (3,-1) C_1…C_2	0.2357	-0.5740	-0.2138	0.0703	-0.0284	-0.4206	-0.4060	0.2525	0.9308	0.7858	0.0358	-37.321
BCP4 BCP84 Type (3,-1) C_7…C_6	0.2313	-0.5680	-0.2049	0.0629	-0.0267	-0.4247	-0.3991	0.2557	0.9405	0.7991	0.0641	-35.155
BCP5 BCP89 Type (3,+1)	0.0052	0.0189	0.0008	0.0038	-0.0030	-0.0024	0.0052	0.0161	0.0137	0.1060	-1.471	-3.938
BCP6 BCP90 Type (3,+1)	0.0363	0.2185	0.0062	0.0484	-0.0423	-0.0291	0.1197	0.1278	0.0531	0.1915	-1.243	-55.529
BCP7 BCP93 Type (3,+3)	0.0048	0.0190	0.0006	0.0040	-0.0034	0.0029	0.0043	0.0012	0.0096	0.0898	-0.320	-4.463
BCP8 BCP98 Type (3,-1) H_{27}…Br_{52}	0.0249	0.0673	-0.0002	0.0170	-0.0017	-0.00252	-0.0245	0.1171	0.1140	0.2641	0.0252	-22.710
BCP9 BCP99 Type (3,+1)	0.116	0.0458	0.0018	0.0095	-0.0077	-0.0100	0.0137	0.0420	0.0306	0.1511	-1.726	-10.108
BCP10 BCP103 Type (3,-1) H_{30}…Br_{52}	0.0229	0.0640	0.0002	0.0157	-0.0155	-0.0228	-0.0215	0.1084	0.1026	0.2527	0.0585	-20.347

Table S6. Drug likeness and ADME properties of PB

Physicochemical properties	
Molecular formula	$C_{22}H_{28}BrN$
Molecular weight	386.37 g/mol
No. of. heavy atoms	24
No. of aromatic heavy atoms	12
Fraction Csp3	0.36
Rotatable bonds	4
H-bond acceptors	0
H-bond donors	0
Molar refractivity	114.16
TPSA	0.00 Å²
Pharmacokinetics	
GI absorption	Low
BBB permeant	No
P-gp substrate	Yes
CYP1A2 inhibitor	Yes
CYP2C19 inhibitor	No
CYP2C9 inhibitor	No
CYP2D6 inhibitor	Yes
CYP3A4 inhibitor	No
Log *K*p (skin permeation)	-4.35 cm/s

Lipophilicity	
Log *P*o/w (iLOGP)	-2.58
Log *P*o/w (XLOGP3)	6.07
Log *P*o/w (WLOGP)	1.76
Log *P*o/w (MLOGP)	1.39
Log *P*o/w (SILICOS-IT)	2.61
Consensus Log *P*o/w	1.85
Water Solubility	
Log S (ESOL)	-6.17
Solubility	2.64×10^{-4} mg/ml; 6.83×10^{-7} mol/l
Class	Poorly soluble
Log S (Ali)	-5.85
Solubility	5.46×10^{-4} mg/ml; 1.41×10^{-6} mol/l
Class	Moderately soluble
Log *S* (SILICOS-IT)	-7.83
Solubility	5.65×10^{-6} mg/ml; 1.46×10^{-8} mol/l
Class	Poorly soluble
Druglikeness	
Lipinski	Yes, 0 violation
Ghose	Yes
Veber	Yes
Egan	Yes
Muegge	No; 2 violations: XLOGP3>5, Heteroatoms<2
Bioavailability score	0.55